



Integrated lithium niobate electro-optic modulators: when performance meets scalability

MIAN ZHANG,^{1,*} CHENG WANG,² PRASHANTA KHAREL,¹ DI ZHU,³ AND MARKO LONČAR³

¹HyperLight, 501 Massachusetts Avenue, Cambridge, Massachusetts 02139, USA

²Department of Electrical Engineering & State Key Laboratory of Terahertz and Millimeter Waves, City University of Hong Kong, Kowloon, Hong Kong, China

³John A. Paulson School of Engineering and Applied Sciences, Harvard University, Cambridge, Massachusetts 02138, USA

*Corresponding author: mian@hyperlightcorp.com

Received 23 November 2020; revised 12 March 2021; accepted 17 March 2021 (Doc. ID 415762); published 7 May 2021

Electro-optic modulators (EOMs) convert signals from the electrical to the optical domain. They are at the heart of optical communication, microwave signal processing, sensing, and quantum technologies. Next-generation EOMs require high-density integration, low cost, and high performance simultaneously, which are difficult to achieve with established integrated photonics platforms. Thin-film lithium niobate (LN) has recently emerged as a strong contender owing to its high intrinsic electro-optic (EO) efficiency, industry-proven performance, robustness, and, importantly, the rapid development of scalable fabrication techniques. The thin-film LN platform inherits nearly all the material advantages from the legacy bulk LN devices and amplifies them with a smaller footprint, wider bandwidths, and lower power consumption. Since the first adoption of commercial thin-film LN wafers only a few years ago, the overall performance of thin-film LN modulators is already comparable with, if not exceeding, the performance of the best alternatives based on mature platforms such as silicon and indium phosphide, which have benefited from many decades of research and development. In this mini-review, we explain the principles and technical advances that have enabled state-of-the-art LN modulator demonstrations. We discuss several approaches, their advantages and challenges. We also outline the paths to follow if LN modulators are to improve further, and we provide a perspective on what we believe their performance could become in the future. Finally, as the integrated LN modulator is a key subcomponent of more complex photonic functionalities, we look forward to exciting opportunities for larger-scale LN EO circuits beyond single components. © 2021 Optical Society of America under the terms of the OSA Open Access Publishing Agreement

<https://doi.org/10.1364/OPTICA.415762>

1. INTRODUCTION

The largest established area of applications in need of improved electro-optic modulators (EOMs) today is at the end of millions of optical fibers in telecommunication and data center optical networks [1]. The original lead in data transport capacity by optical fibers upon their invention has been eclipsed by the continuous progression of electronic bandwidth following Moore's law. In 2020, a single data center application-specific integrated circuit switch passed through 25.6 Tb/s of data, demanding over 400 Gb/s speed for every single lane of optical wavelengths [2]. This data rate is expected to double in the next few years and will continue to grow, driven by technology progression [3]. The pressing need for integrated EOMs for optical communication is to reduce power consumption, while operating at high speed and maintaining an excellent signal-to-noise ratio [4].

Demand for better performance and integrated modulators also comes from emerging applications including satellite data links [5], optical sensors [6], and quantum information processing [7]. These technologies often require electro-optic (EO) functionalities beyond traditional telecommunication applications, such as linearized modulators for analog communications [8], low-loss

switches for quantum communications and computation [9], and integrated modulator arrays for optical neural networks [10].

Large-scale integration and low-cost requirements have led to the rapid development of silicon photonics [11–14]. Leveraging the mature complementary metal–oxide–semiconductor (CMOS) fabrication infrastructure, silicon has become a major commercial photonics platform, in addition to III-V [15] and traditional lithium niobate (LN) systems [16]. While silicon photonics promises excellent scalability and reduced cost, its lack of intrinsic second-order non-linearity [13] presents growing challenges for achieving the required bandwidth and power consumption for future high baud rate systems. High-speed EO effects in silicon often rely on electronic doping, which faces stringent trade-offs between voltage, bandwidth, and optical losses. As a result, various heterogeneous approaches have been explored to introduce better EO solutions for silicon devices [17,18].

The thin-film LN platform could be a practical solution for the next-generation EO photonic integrated circuits (PICs). This platform combines the superior EO properties of industry-proven traditional LN modulators with scalable fabrication techniques such as those used in silicon photonics [Fig. 1(a)]. LN is a

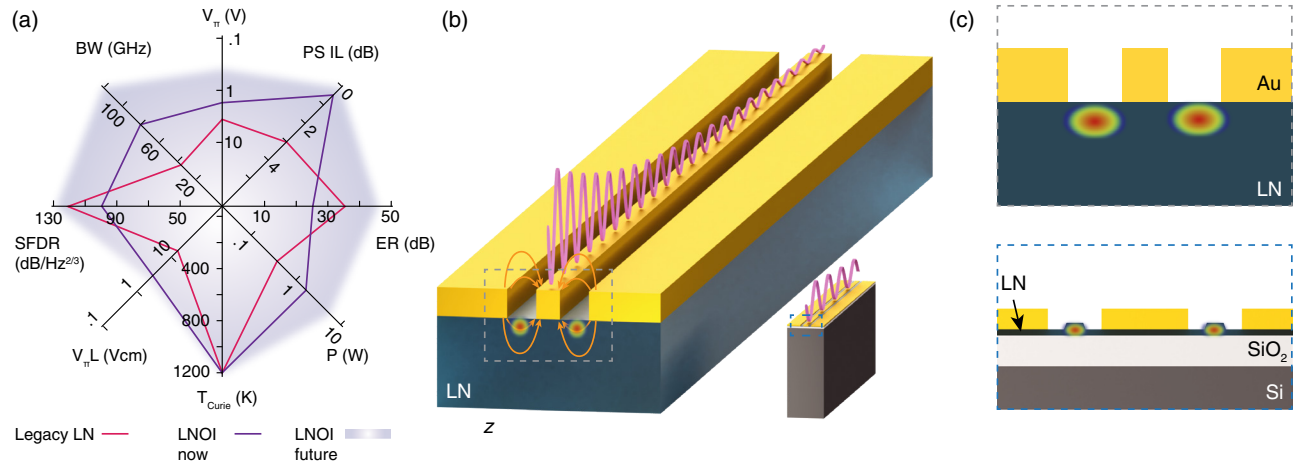


Fig. 1. All-around performance and how it is achieved in a thin-film LN platform. (a) Performance octagon of a modulator designed for telecom wavelength. To reflect the engineering trade-space of the modulator, the curves are chosen to circle performance metrics that can possibly be simultaneously achieved as opposed to individually achieved. The red line corresponds to the typical performance of a commercial bulk crystal LN modulator. The purple line shows the performance of a typical integrated thin-film LN modulator. The blue shaded area is our predicted future performance of an optimized thin-film LN modulator (supporting evidence is discussed in Section 5). V_{π} is the half-wave voltage, which characterizes the power consumption; PS IL is the phase shifter insertion loss, which is the excessive loss in modulation areas; BW is the bandwidth, which describes the operation speed; SFDR is the spurious free dynamic range, indicating the modulation linearity and dynamic range; $V_{\pi} \cdot L$ is the product of the half-wave voltage and phase shifter length showing device size and modulation efficiency; T_{Curie} is the glass transition temperature, which dictates the stability and processability of the electro-optic material; P is the optical power handling capability is the maximum optical power the modulator can hold; ER is the extinction ratio between the on/off states of the modulator. (b) Size comparison of bulk LN devices and thin-film LN devices (aspect ratio not to scale). Longer electrodes usually lead to larger microwave attenuation (purple oscillation) and more challenging velocity matching conditions. (c) Cross section of traditional LN (top) and thin-film LN modulator structures (bottom).

well-understood and established material that has been widely adopted for both optical communications and radio signal processing in its legacy bulk form [16]. With recent technological advances in thin-film material processing and device design, thin-film LN enables modulator performance in previously inaccessible realms and demonstrates significant integration potential. The large gain in performance and the relatively mature understanding of LN could address the immediate optical communication needs and enable future sensors and quantum devices.

We start this mini-review with an overview of the history and evolution of the thin-film LN platform. Next, we explain the working principle and design considerations for various configurations of thin-film LN EOM and discuss their advantages and challenges compared to incumbent technologies. We account for the state-of-the-art achievements and discuss various approaches and figures of merit. We then project future performance metrics that the technology can achieve and lay out our predicted challenges and key milestones. Finally, we take a glimpse at advanced EO circuits that we expect to emerge from the improved modulation capabilities and scalability of thin-film LN.

2. EVOLUTION OF WAVEGUIDE-BASED LN MODULATORS

LN is sometimes referred to as the “silicon of photonics” to emphasize its importance to photonics equivalent to that of silicon in microelectronics. This is because LN possesses many desirable properties for PICs, including a wide optical transparency window, large EO (Pockels) effect, and high glass transition (Curie) temperature, which is critical for process compatibility and maintaining stable operations [19,20]. These superior physical and chemical properties have allowed wide adoption of commercial off-the-shelf

LN solutions as a “workhorse of optoelectronics” [16,21] for decades, which are still widely used at the end of millions of optical fibers today.

For modulators based on the Pockels effect, the key material parameter that dictates the performance is the EO coefficient, r , which describes a linear change in the refractive index in the presence of an externally applied electric field [22]. The largest and most used EO coefficient in LN is $r_{33} = 31$ pm/V [20], which modifies the diagonal optical permittivity (or optical index of refraction). This directly translates into an optical phase shift for light propagating through the material. An external electric field along the crystal z axis E_z changes the extraordinary refractive index n_z [Fig. 1(b)] through the simple relation $\Delta n_z = \frac{1}{2} n_z^3 r_{33} E_z$. This phase shift can be directly used for EO phase modulation or be translated into amplitude modulation using a Mach-Zehnder interferometer (MZI) structure [16].

Legacy LN modulators define optical waveguides by employing proton-exchange or ion-indiffusion techniques to induce a small perturbation in the refractive index of in bulk LN crystalline wafers. These wafers are obtained from LN ingots grown by the Czochralski method. After defining the optical waveguides, electrodes are then placed close to the proximity of the waveguide to apply an electric field to the optical guiding region to induce an index change with an externally applied voltage [Figs. 1(b) and 1(c)]. Long metal electrodes were used to achieve a low drive voltage. They are commonly configured to support traveling wave modulation to circumvent the electrodes resistor-capacitor (RC) bandwidth of the electrodes [Fig. 1(b)]. Such configurations have been studied and optimized over several decades [16,23] and are still used in nearly all commercial LN systems. There are three major limitations in the legacy LN platform: (1) The small index contrast, usually ~ 0.02 , results in large optical

mode sizes exceeding $10\ \mu\text{m}^2$, which limits the positioning of the electrodes and thus limiting the EO modulation efficiency. (2) The high dielectric constant of the LN substrate forces voltage–bandwidth design trade-offs to achieve velocity matching between the microwave and optical signals needed for high-speed operations (e.g., needing a buffer layer and thick metal electrodes). (3) The small optical index contrast results in bending radii well above 1 mm [24] preventing dense integration. The result is that such legacy system is incompatible with the current PIC requirements for performance and integration.

The major roadblocks for achieving high-confinement channel-type optical waveguides in LN, such as those in silicon, were (1) lack of single crystalline thin film and (2) lack of smooth and scalable etching techniques. In the late 90s and 2000s, LN-on-insulator (LNOI) wafers were produced using a similar method to silicon-on-insulator (SOI) wafers through the so-called smart-cut process [25]. An LN wafer was first ion-implanted and then flip-wafer-bonded to a second carrier wafer. The bonded wafer was then annealed to activate the smart-cut process where microexplosions of the implanted ions caused the LN wafers to split leaving a thin film on top of the transferred wafer substrate [26,27]. The bonded LNOI wafer was then polished to achieve atomically flat surfaces and annealed to fix potential crystal damage caused by ion implantation [28]. Notably, thin-film LN can be transferred to silicon substrates with high yield through room-temperature bonding processes [29]. Such LNOI on Si wafers have favorable mechanical properties resembling those of SOIs, making them much more resilient to thermal and mechanical shock than bulk LN substrates. The development and commercialization of LNOI wafers in the late 2000s and the early 2010s (e.g., NanoLN, Partow Technologies, NGK Insulators, TDK Corporation) laid the foundation for the rapid growth of research in high-confinement LN photonics.

Before LN thin films are widely available, etching LN has been carried out to achieve wide and shallow ridge waveguides (e.g., $\sim 8\ \mu\text{m}$ wide $3\ \mu\text{m}$ tall [30]), where the vertical optical mode confinement is still imposed by indiffusion methods. The requirements for etching quality, such as sidewall smoothness, were not as high as those for high-confinement submicrometer structures because of the reduced optical mode to sidewall interaction strength from the wide and shallow waveguide geometry. The growing interest in the development of microphotonic and nanophotonic structures in LN thin films has catalyzed the research on LN dry etching. High-quality dry etching of LN at micrometer scale has been a challenge for years because the non-volatile lithium fluoride byproducts produced from standard fluorine-based etching prevent further etching and cause rough edges [31,32]. With the availability of LNOI wafers, LN nanofabrication techniques have been rapidly developed and iterated. Breakthroughs in LN nanofabrication over the past few years have demonstrated ultralow loss and high-confinement optical waveguides in thin film [31,33–44]. It has been shown that smooth and reproducible etching can be achieved using purely physical methods including argon ion milling or reactive-ion-etching techniques. Optimization of such techniques led to improved optical waveguide loss from initially $>10\ \text{dB/cm}$ and now consistently reaching $<0.3\ \text{dB/cm}$ [35,37–43]. In addition, heterogeneous and hybrid approaches based on rib-loading or chip/wafer bonding have also developed significantly, reaching similar loss levels. These platforms either use hybrid waveguides where the optical modes

are partially confined in the LN thin films or evanescently couple light between the thin-film LN layer and other material layers [29,45–53].

Migrating LN EOMs from their legacy bulk, indiffusion-based waveguides to the nanophotonic, thin-film platform leads to a paradigm shift in the engineering trade-space and enables access to a drastically different performance regime and integration level. It is now possible to simultaneously improve the most desired modulator metrics, including the half-wave voltage (V_π), bandwidth, insertion loss (IL), extinction ratio, power handling, footprint, and linearity [Fig. 1(a)]. Specifically, a thin-film LN modulator made from a wavelength-scale optical waveguide ($\Delta n > 0.7$) allows electrodes to be placed as close as a few micrometers to the waveguide with negligible optical absorption loss [Figs. 1(b) and 1(c)]. A small gap results in a significantly improved EO overlap. The voltage–length product ($V_\pi \cdot L$), which is a commonly used figure of merit to characterize EO efficiency, is much lower in thin-film LN platforms (typically $1.5\text{--}3\ \text{V} \cdot \text{cm}$) [46,50,54–57] than in commercial LN modulators ($\sim 15\ \text{V} \cdot \text{cm}$) [16] at telecom wavelengths (in this review V_π defaults to the push–pull MZI configuration unless otherwise stated). To achieve drive voltages at a much-desired CMOS-compatible level ($1\text{--}2\ \text{V}$ or lower), thin-film LN EOMs only need to be 1 cm long or less [55,56], compared to the $5\text{--}10\ \text{cm}$ long required in legacy forms. With a shorter device, the EO modulation bandwidth can be readily extended to beyond 100 GHz because microwave loss and velocity matching requirements are largely alleviated [50,56,58,59]. In addition, the much-reduced footprint also means a dramatically increased scalability: a commercially available 6-in. wafer can accommodate as many as 3000 EOMs.

We illustrate the overall performance metrics of typical thin-film LN modulators demonstrated thus far (purple line) and traditional LN modulators (red line) in an octagon plot as shown in Fig. 1(a). Considering the large room for improvement from current demonstrations, we further plot the anticipated metrics for future thin-film LN modulators in blue shade, which indicates the possibility of reaching an all-around exceptional performance level. In the following sections, we will discuss the designs that have enabled the improved performances in thin-film LN today and provide evidence and arguments on what could enable the next level of performance.

3. INTEGRATED LN MODULATOR CONCEPTS AND DESIGN

A. Core Modulator Design—Phase Shifter

The design choice for a thin-film LN modulator is centered on increasing the applied electric field strength in the optical mode region while maintaining or improving other desired characteristics. Because LN is an anisotropic EO material, a choice of crystalline cut and the device geometry needs to be made to use the EO effect efficiently. Similar to traditional LN modulators, there are two general categories of modulator design: one with the crystal axis (z axis) in plane with the wafer, that is x -cut or y -cut, and the other with the crystal axis out of plane, that is z -cut (Fig. 2).

In an x -cut design (this also includes any other cuts along the z axis in plane), the strongest component of the applied electric field should be designed to align with the in-plane z axis of the crystal to utilize the largest r_{33} component [see Fig. 2(a)]. In this geometry, the guided optical mode, which experiences a refractive

index change due to the applied electric field, is placed between a pair of electrodes with opposing polarities. To place metal electrodes close to each other on a thin-film LN, a rib/ridge type of structure [Figs. 2(a)–2(c)] is commonly used to introduce strong confinement of the optical mode. Light is usually launched in transverse electric modes such that the optical field aligns with the strongest external applied field.

There are two variations to define the ridge: a “monolithic” approach where the rib structure and the slab are formed from a single piece of LN [Fig. 2(a)] by etching, polishing, or dicing; and a hybrid approach where the rib is formed by another high-refractive-index guiding material [Figs. 2(b) and 2(c)], which avoids direct patterning of the LN thin-film. The LN slab is necessary for both approaches and is a key part of the x -cut phase shifter design. In the monolithic approach, a thin slab dramatically reduces the effective electric field in the LN rib area because of the large permittivity contrast between the LN ($\epsilon_{\text{LN}} = 28$) and the surrounding optical cladding (e.g., $\epsilon_{\text{SiO}_2} = 3.8$). This leads to a large voltage drop in the passive dielectric outside the LN core region, as dictated by the boundary condition of the electric displacement fields [50,56]. A thick slab leads to weak optical confinement and results in a larger bending radius and wider electrode gaps. In the hybrid approach, an LN slab is necessary to enable EO modulation. A well-engineered ratio between the slab and rib thicknesses for hybrid structures is important for maximizing the modulation efficiency while achieving reasonable optical confinement and minimal bending radius [60]. While optimizations can be made for various performance priorities, the index contrast between the LN and cladding ultimately dictates the achievable level of optical confinement, resulting in typical DC $V_{\pi} \cdot L$ values of 1.5–3 V · cm [46,50,54–57].

In a z -cut LN modulator design, the strongest component of the applied electric field required is out-of-plane [Figs. 2(d)–2(f)]. To achieve efficient modulation, the guided optical mode is positioned underneath the signal electrode and light is launched in transverse magnetic modes to align with the strongest component of the external applied field. A low-index buffer layer (e.g., SiO₂) between the optical waveguide and electrode is typically required

to prevent excessive metal absorption losses. The ground electrodes are placed on both sides of the optical waveguides [Fig. 2(d)] to create a strong vertical component of the electric field in the optical mode region. Note that a thin-slab layer is still typically preferred in this z -cut design to facilitate electric field penetration through the high-permittivity LN sections. It is also feasible to locate the ground electrode below the optical waveguide to form a vertical capacitor [Fig. 2(e)] [61,62], which can be realized using an LNOI wafer pre-embedded with a bottom metal layer. However, this configuration may be challenging in achieving optimum microwave properties at high frequencies owing to the large capacitance between the signal electrode and the large ground plane. Hybrid methods can also be applied to z -cut LN designs. For example, an LN film can be bonded on top of the already formed optical waveguides and electrodes [48,51,59]. A signal electrode can then be patterned on top of the LN film to achieve a strong vertical electric field. In this case, depending on the slab material index and optical loss that can be tolerated, the buffer layer between the LN film and the top electrode can be made much thinner or even eliminated to achieve a strong vertical electric field.

We provide several numerical examples of the calculated $V_{\pi} \cdot L$ for each phase shifter design at telecom wavelengths. Our simulations (see Table 1, Appendix A) showed $V_{\pi} \cdot L$ values ranging from 2.05 V · cm to 5.4 V · cm for x - and z -cut designs where metal-induced optical loss is kept at a minimum. This agrees with the range of measured values previously reported. Importantly, we provide these quantitative examples as a starting point for each design, not as proof of the final optimized device performance. For example, shallower ridges could be used to push the modes more into LN slab region to achieve higher efficiency; electrode gaps may be reduced to increase EO modulation efficiency using a low-index dielectric buffer layer or at the cost of slightly increased optical loss. In addition, radio frequency (RF) properties such as impedance and loss, and practical utility considerations such as fabrication tolerance, could outweigh minor $V_{\pi} \cdot L$ value differences, as discussed below.

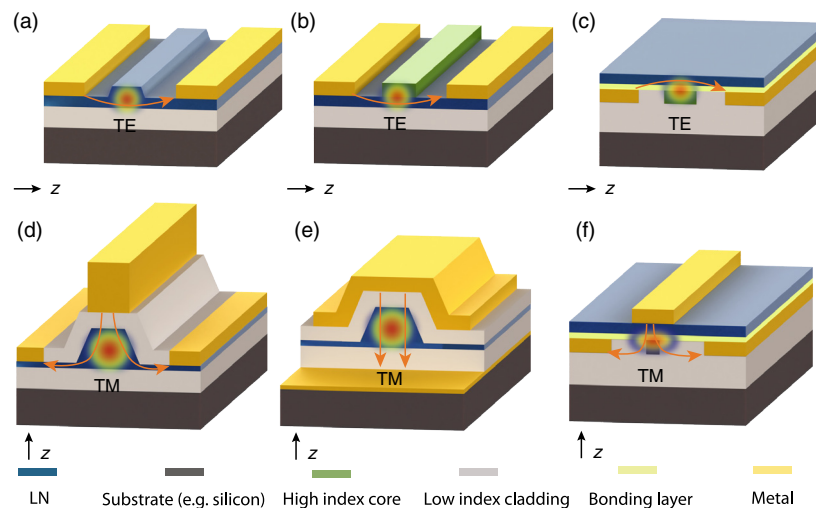


Fig. 2. Electrode configurations for x - and z -cut lithium niobate (LN) modulator design. The orange arrows indicate the applied electric fields direction, the shaded area indicates the location of the optical mode, TE is the transverse electric mode, and TM is the transverse magnetic mode. (a) All-LN x -cut rib waveguide design; (b) hybrid strip-loaded x -cut ridge waveguide design; (c) hybrid buried waveguide x -cut with inverse ridge design; (d) all-LN z -cut rib waveguide design with planar electrodes; (e) all-LN z -cut rib waveguide design with buried ground plane; (f) hybrid z -cut waveguide with inverse ridge design.

B. MZI and High-Speed Electrode Design

To turn the phase shifter into a high-speed intensity modulator, a traveling wave MZI is commonly used. In an MZI modulator (MZM), the input light beam is split into two paths and an optical phase difference between the two arms is induced using the EO phase shifters, resulting in a change in the output intensity when the two paths are combined. A common method to reduce the single-arm $V_\pi \cdot L$ value by a factor of 2 is to use a push-pull electrode design in which the phase of one arm is advanced while the other is delayed.

In a traveling wave MZM [16] [Fig. 1(d)], it is critical to satisfy the velocity matching condition: the optical wave needs to travel at the speed of the electrical signal. When the optical group and electrical phase velocities are matched [16], the modulation effect can continue to accumulate as long as (1) such a velocity matching condition is maintained, (2) the microwave signal is not heavily attenuated, and (3) the impedance of the RF transmission line matches well with the external electronics allowing efficient microwave delivery.

For x -cut devices, the convenient in-plane electrode-waveguide geometry allows the pair of optical waveguides to be placed right inside the dielectric gaps of a standard ground-signal-ground (GSG) microwave coplanar waveguide [63,64] [Fig. 3(a)], where the electric fields across the two optical waveguides are pointing in opposite directions. Such a configuration is desirable because, in addition to reducing $V_\pi \cdot L$ by a factor of 2, it also offers symmetric modulations of the two arms of the MZI to minimize the modulation chirp. This is important to preserve signal integrity when propagating through long optical fibers [65]. Traditionally, x -cut designs have been challenging in matching RF and optical velocities. A buffer layer and thick electrodes ($>10 \mu\text{m}$) are often used to pull the RF mode out of the high-permittivity LN crystal to speed it up [16], at the cost of reduced EO modulation efficiency. In thin-film x -cut designs, velocity matching and low RF loss can be achieved with a thin metal layer ($\sim 1 \mu\text{m}$) and without dielectric buffer layers, using a low-permittivity substrate such as SiO_2 ($\epsilon_{\text{SiO}_2} = 3.8$) on Si ($\epsilon_{\text{Si}} = 11.7$). Such design flexibility of the x -cut thin-film LN makes it a popular crystal cut choice and provides ample space for further optimization [56,66].

Z -cut electrodes do not readily support a symmetric push-pull configuration for a single electrical drive, such as the x -cut/ y -cut EOMs. Push-pull modulation on a z -cut thin-film can be achieved using a configuration similar to a z -cut bulk EOM. The two optical waveguides are placed under a signal and a ground electrode, respectively, as shown in Fig. 3(b). In this configuration, the electric field strength experienced by the optical waveguide underneath the ground electrode is typically 3–10 times weaker than that experienced by the waveguide underneath the signal electrode [16], leading to significant chirp, which is likely exacerbated for ridged structures in thin-film LN owing to the stronger electric field

gradient. Alternating electrode placement relative to waveguides and crystal domain inversion may be needed to achieve chirp-free operation [67].

Z -cut geometries present a convenient and compact way to implement a dual-drive (or differential drive) configuration, as shown in Figs. 3(c) and 3(d). Figure 3(c) shows a differential GSGSG electrode configuration where the two signal lines have opposite voltages, capable of delivering a symmetric chirp-free modulation. It is possible to further reduce the V_π value using a differential and push-pull GSSG design because the field between the positive and negative signal lines can be stronger [Fig. 3(c)]. Although such configurations have not yet been adopted in thin-film LN, we believe that differential driving is a feasible future route because differential driver circuitry is widely accessible commercially. Furthermore, differential transmission line pairs feature improved RF shielding between devices in proximity, which may be beneficial to further reduce the device footprint. While the signal line thickness, gaps, and substrate can be readily engineered in z -cut designs, the signal linewidths in Figs. 3(b)–3(d) have a limited tuning range without changing the electrode gaps, unlike the x -cut. This could lead to more trade-offs between EO efficiency, RF loss, and impedance. To minimize the ohmic losses while preserving high EO efficiencies, a signal line with substantial thickness may be required, as shown qualitatively in Figs. 3(b)–3(d). In addition, LN films can accumulate substantial charges on the z -surface under temperature fluctuations due to pyroelectricity [68]. A charge bleed layer may be required in z -cut devices to prevent surface discharge or significant bias point drift.

Both x - and z -cut designs can achieve a significantly higher EO bandwidth than traditional LN EOMs because they have shorter electrodes. The velocity mismatch limited bandwidth increases linearly with a reduction in the electrode length. In bulk LN, velocity matching beyond 40 GHz can be routinely realized on a 5 cm long electrode with a V_π of 3 V [16]. To achieve the same voltage, a 7 mm electrode on thin-film LN is needed which would have a velocity matching limited bandwidth >280 GHz. Moreover, the multilayer structure in a thin-film LN structure, for example, consisting of an LN device layer, SiO_2 bottom cladding, and Si substrate, allows independent tuning of the RF velocity by designing the thickness of the SiO_2 cladding without sacrificing the EO overlap.

Current thin-film LN EOMs are mainly limited by the ohmic loss of RF electrodes at microwave frequencies. The ohmic loss (O) of a typical coplanar transmission line follows a square root dependence of the microwave frequency f due to the skin effect and a linear dependence on length L , that is, $O = \alpha_o f^{1/2} L$, where α_o is the ohmic loss attenuation coefficient in units of $\text{dB} \cdot \text{cm}^{-1} \cdot \text{Hz}^{-1/2}$. Because the 3 dB EO bandwidth corresponds to the frequency at which the transmission line electrode has a loss of $O \sim 6.4$ dB assuming the velocity

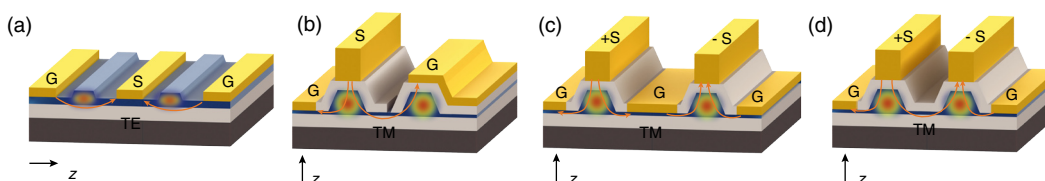


Fig. 3. Microwave electrode designs for several intensity modulator configurations. (a) X -cut lithium niobate (LN) typically uses a symmetric design with a ground-signal-ground (GSG) configuration to create a natural push-pull modulation. Z -cut LN may use (b) a GSG push-pull driving configuration, (c) a GSGSG configuration, or (d) a GSSG differential driving configuration.

is matched [68–70], we can derive an estimated ohmic loss limited bandwidth as $f_{3\text{-dB}} \sim (6.4/\alpha_o V_\pi \cdot L)^2 V_\pi^2$. Evidently, breakthrough in $V_\pi \cdot L$ (from 15 to 2 V·cm) has been the main driver for thin-film LN modulators to realize higher EO bandwidths. It is noteworthy that typical RF losses in current thin-film LN modulators $\alpha_{o,\text{TF}} \sim 0.7 \text{ dB} \cdot \text{cm}^{-1} \cdot \text{Hz}^{-1/2}$ are substantially higher than that of commercial bulk LN modulators $\alpha_{o,\text{BK}} \sim 0.2 \text{ dB} \cdot \text{cm}^{-1} \cdot \text{Hz}^{-1/2}$ [23], due to reduced metal gaps and thinner electrodes. Taking typical values for both cases, we obtain $f_{3\text{-dB,TF}} \sim 21 V_\pi^2 \text{ GHz V}^{-2}$ for thin-film LN EOMs and $f_{3\text{-dB,BK}} \sim 4.5 V_\pi^2 \text{ GHz V}^{-2}$ for bulk LN EOMs, representing more than 4 times improvement in bandwidth for the same driving voltage on the thin-film platform.

4. STATE OF THE ART

Since the realization of wavelength-scale waveguides in thin-film LN [26,61,62,71,72], modulators have been a key topic of research interest. Earlier works demonstrating the EO effect of thin-film LN use z -cut geometries with buried ground electrodes [Fig. 2(e)] [61,62]. The fabricated devices typically have modulation efficiencies of $\sim 15 \text{ V} \cdot \text{cm}$ (for MZI) and 1 pm/V (for microresonators), which is probably limited by imperfect device design [61,62]. The optical propagation loss of these demonstrations also remained relatively high particularly for narrower waveguides, owing to the challenge in LN etching at the time.

In the past decade, x -cut designs have become increasingly popular, especially because low-loss hybrid/heterogeneous devices have been demonstrated to circumvent the LN etching challenge. Using the x -cut geometry shown in Fig. 2(b), a heterogeneous LN modulator with a silicon nitride ridge waveguide on thin-film LN was demonstrated in 2013, featuring a V_π of 6.8 V and a $V_\pi \cdot L$ product of 4 V·cm [29]. This demonstration significantly surpassed the $V_\pi \cdot L$ of typical commercial LN modulators. In 2016, this heterogeneous design was further improved to include traveling wave electrode designs, demonstrating a V_π of 3.9 V with an optical loss of 1.2 dB/cm [57]. More importantly, the device featured a 3 dB bandwidth of 33 GHz and a 6 dB bandwidth of 50 GHz, showing that the dramatically improved DC modulation efficiency can be extended to RF frequencies [Fig. 4(a)]. In the same year, an all-LN inverse ridge modulator was reported featuring a usable bandwidth of up to 110 GHz (3 dB bandwidth of 40 GHz) [73] with $V_\pi = 9 \text{ V}$ and propagation loss of 7 dB/cm. The demonstration showed that fundamentally LNOI could work for modulation frequencies beyond 100 GHz [73]. The $V_\pi \cdot L$ product of x -cut devices was later improved to 1.8 V·cm using the monolithic approach with a gap of 3.5 μm [Fig. 2(a)] [54]. The device uses a lumped capacitor design and is therefore limited to a relatively low bandwidth of 15 GHz by the RC time constant even with a short device length of 2 mm, which also resulted in a high V_π of 9 V [54]. The 3 dB/cm optical loss is improved from previous devices but is still quite significant.

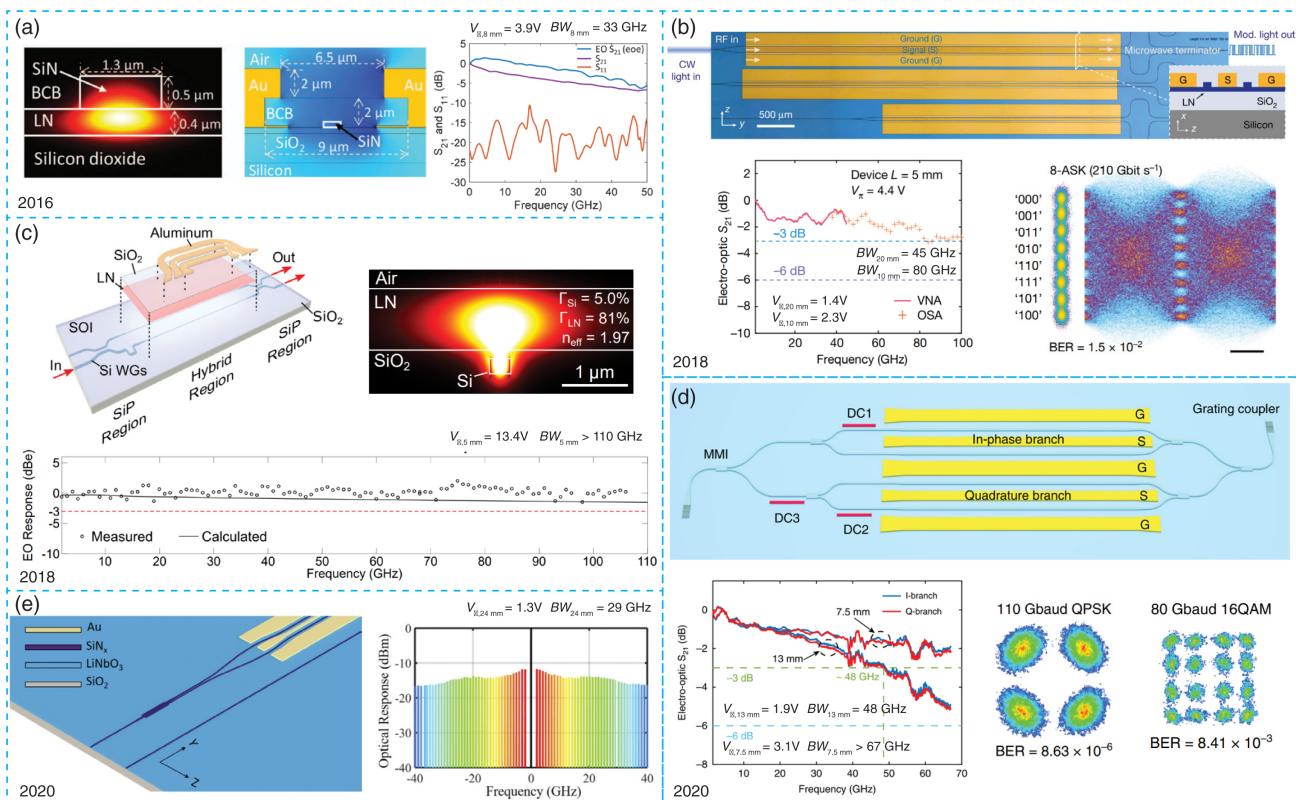


Fig. 4. Representative demonstration of integrated lithium niobate (LN) modulators. (a) Heterogeneously integrated LN modulator with silicon nitride (SiN) as guiding strip on top of LN [57], with permission from The Optical Society of America. (b) Low-voltage and high-bandwidth monolithic modulator [56], reprinted by permission from Springer Nature. (c) Heterogeneously integrated ultrahigh bandwidth thin-film LN bonded on silicon-on-insulator (SOI) wafers [59], with permission from The Optical Society of America. (d) Coherent in-phase and quadrature (IQ) modulators achieved on monolithic platform [74], licensed under a Creative Commons Attribution (CC BY) license. (e) Low-voltage SiN on LN thin-film heterogeneous modulator [75], licensed under a Creative Commons Attribution (CC BY) license.

An efficient z -cut design on LN thin films heterogeneously bonded to SOI wafer was demonstrated in 2013 [76]. Here, the geometry shown in Fig. 2(f) was used in the form of a microring resonator. The tuning efficiency achieved is 12.5 pm/V, translating into a voltage–length product of about $3.7 \text{ V} \cdot \text{cm}$, which could be further reduced to $1.8 \text{ V} \cdot \text{cm}$ if a push–pull differential drive is used. It should be noted that this high tuning efficiency was achieved at low frequencies by directly using the silicon ridge as the bottom electrode, which may require a more optimized design to operate at high frequencies [76]. The later demonstration from the same group shows an RC-limited 3 dB bandwidth of 5 GHz, but with a reduced tuning efficiency of 3.3 pm/V since the transverse electric mode and the r_{13} component were used.

Breakthroughs in the fabrication of low-loss LN waveguides in 2017 and 2018 [35–38,44] and the potential for a better $V_\pi \cdot L$ spurred new interest in monolithic LN modulators, in particular with x -cut designs, owing to the fabrication and microwave design convenience. Using an LN thin film on a quartz substrate and the geometry shown in Fig. 2(a), a modulator with a V_π of 1.5 V, a voltage–length product of $2.2 \text{ V} \cdot \text{cm}$, and a 3 dB bandwidth of 20 GHz is produced, with usable bandwidths of up to about 45 GHz [77]. Using better velocity-matched traveling wave designs and a low-loss optical waveguide, a monolithic single-drive LN modulator with a V_π of 1.4 V, a 3 dB bandwidth of 45 GHz, and an on-chip loss of $\sim 0.5 \text{ dB}$ [Fig. 2(a) configuration] has been demonstrated [56]. In the same series of devices, modulators with 3 dB bandwidths as high as 100 GHz have been achieved with a relatively low half-wave voltage of 4.4 V [56] [Fig. 4(b)]. At the same time, a novel hybrid approach was demonstrated. Silicon waveguides are used for most of the passive parts of the PIC and when EO modulation is needed, the optical mode is fully transferred into a dry-etched thin-film LN rib waveguide [50]. This hybrid/monolithic approach allows the integration of LN modulators with silicon photonics while maintaining essentially low $V_\pi \cdot L$ products ($2.2 \text{ V} \cdot \text{cm}$). Heterogeneous platforms using the configuration shown in Fig. 2(c) have also shown modulators with a high 3 dB bandwidth $> 106 \text{ GHz}$ while having a moderate driving voltage of 13 V ($V_\pi \cdot L = 6.8 \text{ V}$) [59]. Most recently, more complex in-phase and quadrature (IQ) modulators for coherent communications have also been demonstrated, with each IQ arm featuring a similar level of performance to single modulators [Fig. 2(a) configuration] [74] [Fig. 4(c)], all exceeding those of commercial modulators in bandwidth and driving voltages. It should also be noted that with optimized design, heterogeneous

modulators have also achieved low V_π of 1.3 V while maintaining a 3 dB bandwidth of 29 GHz [75] [Fig. 4(e)].

In comparison to x -cut designs, z -cut modulators have been experimentally explored much less so far despite our prediction of a similar or even better $V_\pi \cdot L$. We believe this is due to the more demanding processing requirements such as the need for a deeper LN etch for the z -cut monolithic approach. A recent work using a z -cut design showed an excellent tuning efficiency of 20 pm/V at DC and 9 pm/V at RF frequencies [78]. For the heterogeneous approach, a metal electrode must be deposited on top of the bonded LN thin film. Such post-processing requirements could compromise CMOS compatibility, possibly reducing the attractiveness of this approach. As processing techniques advance, we anticipate that more z -cut modulators will appear owing to the future due to the inherent advantages of the z -cut approach in terms of differential drive and in-plane bending electrodes.

To visualize the rapid evolution of thin-film LN modulators, we put the currently achieved performance metrics in two important parameter trade-spaces shown in Fig. 5 (see also Table 2, Appendix A): phase shifter loss versus voltage and bandwidth versus voltage. We also selected a few recent representative works from other popular modulator platforms and compared their performances with thin-film LN EOMs. From Fig. 5(a), we can see that thin-film LN EOMs lead with a large margin compared to many other platforms. Such low-voltage and low phase shifter loss modulators are critical for scaling up the complexity of integrated EO circuits. Regarding voltage–bandwidth performances [Fig. 5(b)], we can see that thin-film LN modulators are already on a par with, if not outperforming, most other on-chip platforms and commercial bulk LN modulators that have been optimized for decades.

Monolithic LN ridge modulators have slightly better overall performance than hybrid ones, but a more comprehensive evaluation must be made to consider the right platform for future applications. A strong motivation for a hybrid approach is to allow thin-film LN to be used in the wafer backend processes of silicon photonics processing technology. This would allow one to harness the extensive photonics libraries built for the silicon photonics [41,71]. Here, the key is to design the LN processing to take place as close to the end of the silicon waveguide fabrication cycle as possible, for example after wafers are freed from the CMOS fabrication steps. One can directly transfer (stamp) LN films, either in the form of an entire wafer or smaller pieces, onto waveguides predefined in other photonic materials including silicon [e.g., Fig. 2(c)].

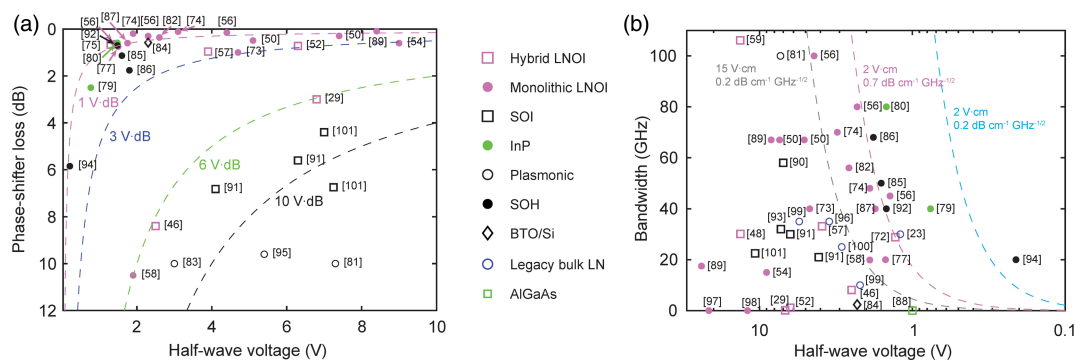


Fig. 5. State-of-the-art performance comparison between thin-film lithium niobate (LN) and other platforms using data from previous research. (a) Phase shifter loss and half-wave voltage trade-off, with data from [29,46,50,52,54,56–58,73–75,77,79–95]. Dashed lines show voltage–phase shifter loss trade-off curves. (b) Voltage–bandwidth trade-off, with data from [23,29,46,48,50,54,56,58,59,74,75,79–81,84–94,96–101]. Dashed lines represent the expected voltage–bandwidth performance for a given electrode modulation efficiency and transmission line loss.

5. PERFORMANCE PROSPECTS OF FUTURE LN MODULATORS

Considering the short history of thin-film LN modulator development, it is reasonable to expect further improvements in almost all key performance areas. In this section, we discuss the required design and advances in fabrication. We envisage future integrated LN modulators will simultaneously achieve CMOS-level drive voltage, bandwidth exceeding 100 GHz, on-chip loss <0.5 dB, optical power handling at the watts level, linear EO response, extinction ratio >50 dB, and excellent stability [Fig. 1(a)]. Here we focus our discussion for telecom wavelengths (e.g. 1.55 μm). For shorter wavelength applications such as 1.3 μm and visible wavelengths, thin-film EOMs are expected to have even better voltage-bandwidth performance due to the reduced phase shift requirement and better optical confinement for further reduced electrode gaps.

A. Voltage and Bandwidth

There is substantial room to improve the voltage–bandwidth performance of LN EOMs much beyond what has been demonstrated today [blue dashed curve in Fig. 5(b)]. To overcome the dominating ohmic loss in transmission line electrodes, design concepts including thick and asymmetric electrodes are being explored [66,102,103]. Recently, EOMs with $0.26 \text{ dB} \cdot \text{cm}^{-1} \cdot \text{Hz}^{-1/2}$ electrode loss on thin-film LN have been experimentally demonstrated while maintaining $V_\pi \cdot L$ of $2.3 \text{ V} \cdot \text{cm}$ using microstructured electrodes [104], corresponding to an ohmic loss limited EO bandwidth of $114 \text{ V}_\pi^2 \text{ GHz V}^{-2}$. This points to possible future modulators with a half-wave voltage of <1 V and a 3 dB bandwidth over 100 GHz simultaneously [Fig. 1(a) BW and V_π axes].

At frequencies approaching or extending beyond 100 GHz, other sources of RF losses including linear dielectric absorption loss and substrate radiation loss should also be considered. LN crystals have a relatively low-loss tangent of 0.004 [105] and can be bonded to near-ideal microwave substrates such as quartz. In the configuration reported in [104], RF absorption loss is expected to contribute less than 15% of the total electrode loss up to 200 GHz. Substrate radiation loss is also significantly suppressed in thin-film LN EOMs owing to the better confined microwave mode from the reduced electrode gap. Experimental demonstrations with up to 500 GHz usable bandwidth have been reported [58] in contrast to bulk LN modulators that face strong attenuation from substrate radiation beyond 70 GHz. Detailed contributions in thin-film LN from each loss channel across different substrates would require further theoretical and experimental investigations.

B. Size

The footprint of a thin-film LN modulator is ultimately limited by the $V_\pi \cdot L$ product, which translates into a size requirement for achieving a certain drive voltage. We believe that the current demonstrated $V_\pi \cdot L$ product of $1.5\text{--}3 \text{ V} \cdot \text{cm}$ for thin-film LNs faces strong challenges for large improvement [Fig. 1(a), $V_\pi \cdot L$ axis], without significant trade-off with optical loss and/or microwave loss. It is possible to further improve $V_\pi \cdot L$ without sacrificing optical loss by introducing new materials. For example, a dielectric cladding with a low optical index and high RF permittivity can facilitate electric field penetration into etched LN ridges

without compromising optical confinement. Using magnesium oxide (MgO) as a cladding material, which has an optical refractive index of ~ 1.7 , and RF permittivity of 10, the DC $V_\pi \cdot L$ in the x -cut configuration could be reduced compared to that with a SiO_2 cladding. However, other factors such as the RF loss, design changes (e.g., impedance and velocity matching), and process compatibility should be carefully evaluated.

With a somewhat limited room for $V_\pi \cdot L$ improvement, the length of the thin-film LN modulator active area will likely remain at the millimeter to low centimeter scale to achieve a balanced bandwidth and voltage performance. Such $V_\pi \cdot L$ is comparable to reverse-biased high-speed silicon modulators [91,93,101,106], although it is sometimes significantly larger compared with other modulator technologies such as indium phosphide (InP) [79,80], silicon-organic hybrid [85,86,92,94], and plasmonic platforms [81,83,95]. For thin-film LNs, a 5 mm long modulator would have a $V_\pi \sim 4 \text{ V}$ but with a bandwidth >100 GHz and negligible phase shifter loss. This is to be compared to $V_\pi \sim 6.3 \text{ V}$, 30 GHz bandwidth, and >5 dB phase shifter loss for a Si modulator with the same size [91]. The significant performance advantage of a thin-film LN relative to a silicon modulator is clear. However, to fully exploit the low-voltage and low-loss properties of thin-film LN devices (e.g., V_π of $\sim 1 \text{ V}$), electrodes as long as 20 mm would be of interest [55]. For applications that are sensitive to package lengths such as optical transceivers, the electrodes can be wrapped around to reduce the overall length while maintaining a small area, taking advantage of the small bending radii available in both x - and z -cut thin-film LN platforms.

C. Optical Insertion Loss

The LN phase shifter loss has shown the potential to reach <0.03 dB/cm [35,40] [Fig. 1(a), PS IL axis]. Achieving this value is important for cascaded or ultralow-voltage devices. For standalone modulators, the dominant source of optical insertion loss is the coupling between the LN and the optical fibers. In principle, the hybrid approach can leverage the silicon photonics component library and achieve <1 dB/facet coupling loss [106]. For the monolithic approach, inverse tapers and grating couplers have been demonstrated to alleviate optical mode mismatch with standard optical fibers. Because the refractive index of LN is close to that of silicon nitride, it is reasonable to believe that a similar interface loss can be achieved compared with silicon nitride. So far inverse tapers-based designs have allowed fiber-to-chip coupling loss as low as 1.7 dB/facet [107–109] and 0.52 dB/facet more recently [110]. Grating couplers directly etched in LN have also shown efficiencies of the order of 3.5 dB/facet [111–114]. Gratings made in the amorphous silicon layer deposited on top of LN have been shown in theory enabling a total fiber-to-fiber loss of $\sim 1.4 \text{ dB}$ [115]. Considering the low on-chip loss already demonstrated, integrated modulators with an overall fiber-to-fiber insertion loss of <2 dB can be envisaged. Such an achievement would be a significant milestone for both classical communication and quantum photonics.

D. Extinction Ratio

A high extinction ratio is desired for many applications including optical switching, quantum photonics, and metrology. Current thin-film LN modulators typically have 20–30 dB and sometimes up to 40 dB extinction ratio on the chip [50], which can compete

with mature integrated photonics platforms. Importantly, the absorption coefficient of LN does not change with an external modulation voltage, fundamentally avoiding the coupling between the real and imaginary parts of the refractive index that leads to the degradation of the extinction ratio commonly seen in silicon [13] and InP modulators [15]. While the limiting factor of the extinction ratio in thin-film LN EOMs has not been fully explored, it is believed to be due to non-optimized waveguide [116], beam splitter designs, and/or fabrication imperfections [117]. Furthermore, the excellent scalability of the LN platform allows more complex configurations such as cascaded MZI [118] to increase the extinction ratio to >50 dB with a small overhead on the device footprint [Fig. 1(a) ER axis].

E. Linearity

Modulation linearity is an important performance metric for analog links and digital multilevel modulation schemes [119]. Traditional LN is known for its excellent linearity performance because the refractive index (hence optical phase) shifts linearly with external electric field in the Pockels process. The linearity of an LN modulator is mostly limited by the non-linearity of the sinusoidal transfer function of the MZI [120]. Only a few experiments have been carried out in thin-film LN to measure important linearity metrics such as spurious-free dynamic range (SFDR) [48,50,60,121]. These initial results have shown promising performance numbers (third-order intermodulation of the SFDR up to ~ 100 dB \cdot Hz^{2/3}) when compared to traditional LN modulators under similar measurement conditions (e.g., input power and noise floor) with room for improvement. The current numbers are likely limited by the relatively high insertion loss due to non-optimized fiber–chip coupling and non-ideal noise baseline during testing. Improving the overall link loss using the techniques discussed in the previous section will likely lead to better a SFDR performance. Even more exciting is that the integrated LN platform readily allows more complex linear modulation schemes to be integrated in a small footprint, such as ring-assisted MZIs [8] or cascaded MZIs [122], which could provide the best in-class linearity performances comparable to or beyond what has been achieved on bulk LN [Fig. 1(a) SFDR axis].

F. Photorefractive and DC Drift

Crystalline Pockels materials such as LN, are subject to effects such as photorefractive. When a defect in the crystal is excited by light, it creates a spatial charge field that can have a macroscopic lifetime of the order of seconds to even hours due to limited material conductivity [123]. The spatial charge field induces an undesired effective EO phase shift, which can lead to bias drift in the modulator. This behavior can become even more complicated when an external DC bias field is present [124,125]. In this case, the photoinduced space charge not only creates a field that can cancel the external DC bias, but also varies in time and depends on optical intensity. This is because the spatial charge distribution is determined by a dynamic balance between photoinduced charge generation and photoconductive charge redistribution.

There are several ways to address this challenge. First, the photorefractive effect quickly rolls off for high-frequency signals (>1 MHz) for thin-film LN EOMs, limiting the impact to low-frequency applications and long-term drifts [126,127]. Historically, photorefractive and DC bias drift problems in LN

have been addressed through various buffer layer material choices for faster dissipation of the charge buildup, as well as external feedback bias controllers [16]. For thin-film LN, research in these areas, especially long-term stability tests, has been limited so far. The low-frequency and long-term performance of thin-film LN modulators could be further improved by adopting approaches similar to those used in bulk LN, as well as surface treatment and cladding material optimization.

In thin-film LN, thermo-optic phase shifters can also be used for DC bias control with relatively simple designs. Initial evidence suggests that heater-based DC phase shifters can be more stable than EO phase shifters in thin-film LN EOMs [74,128]. Nevertheless, the relatively high electrical power consumption (tens of milliwatts) could be unfavorable for power-sensitive applications. Because LN is also an excellent piezoelectric material, methods such as electro-mechanical tuning, which can be of extremely low power consumption and independent of optical intensity, can also be attractive solutions [129]. Alternatively, DC bias can be controlled on mature material platforms such as silicon using heterogeneous approaches [50].

G. Power Handling

In traditional LN components, photorefractive can also cause significant optical damage at high optical powers >1 W at telecom wavelengths [16,123]. Photorefractive damage can be even worse in the visible range, where many devices are often made with MgO-doped LN crystals to counteract photorefractive. Intuitively, the power handling capability of thin-film LN EOMs could be more problematic, because the optical power density is increased by as much as 100 times when the optical mode diameter is reduced from ~ 10 μ m to <1 μ m. However, as demonstrated experimentally in microring resonators [39,43,107], estimated circulation powers of up to 150 W at telecom and mid-infrared wavelengths have been achieved without inducing damage to the waveguides, even for congruent LN films without MgO doping. The damage threshold of thin-film LN devices at visible wavelengths has not been studied in detail, but is likely to also be higher than bulk LN, considering that significant amounts of second-harmonic and third-harmonic powers have been observed in non-linear optical devices [43,130]. While photorefractive is still present in thin-film LNs and can cause device instability for microresonators at intermediate optical power levels [126,127,131,132], it has a saturation effect beyond a certain power level [133], allowing room temperature use at high input optical powers. Based on the waveguide circulation powers observed in microring resonators, an EOM capable of 10 W-level optical power handling can be envisaged if fiber-to-chip coupling can be designed to handle such optical power [Fig. 1(a) P axis]. Although the better power handling in thin-film LN is not fully understood yet, one possibility is that the largely increased index contrast diminishes the effect of photorefractive, which can be detrimental for traditional systems with index contrasts <0.02 . For high-power or visible applications where the photorefractive effect is expected to be stronger, materials with similar properties to LN but less photorefractive effect such as lithium tantalate (LiTaO₃) or MgO-doped LN can be used [134,135]. In particular, LiTaO₃ has a similar EO coefficient to LN while simultaneously having a cutoff frequency of 280 nm [136]. The significantly increased power handling capability is very important for analog photonics links to achieve the desired gain and noise figures [119].

H. Scalability

The next question is the scalability of integrated LN EO circuits, and whether these PICs can maintain the performance edges while scaling up. The scalability and manufacturability fundamentally dictate the practical functionality and cost of PICs. Heterogeneous bonding of LN film to existing platforms such as SOI can be readily scaled up to large sizes if a reliable and cost-effective backend process can be developed [48,137]. A major challenge here is how to preserve the performance advantage with limitations on the design space imposed by the backend compatible integration process.

At the same time, exciting developments of the front-end processing of LN enables complementary solutions in the monolithic approach. LNOI wafers are now commercially available at up to 6-in. diameter, with an 8-in. diameter possible in the foreseeable future [138]. Recently, it has been shown that a low optical loss of <0.3 dB/cm can be consistently achieved across 6-in. thin-film LN wafers using mass production techniques such as deep ultraviolet lithography [41]. This shows that high EO performance metrics can be achieved on the wafer scale while maintaining low cost and high yield. While the silicon photonics industry can produce chips in extremely large volumes, many photonics applications, including telecommunications, only require a small fraction of the volumes compared to electronics. Therefore, smaller wafers for LN may still hold the potential to address these challenges with their performance advantage and potential low cost.

Because the LNOI platform has excellent passive and EO components, it is also possible to think about integrating lasers and detectors on LN using similar heterogeneous integration approaches developed for silicon photonics to achieve full photonic modality with ultrahigh performance. In addition, the versatile material properties of LN can enable additional integrated LN functionalities. For example, non-linear optical processes can be efficiently realized in periodically poled LN [53,130,139–141]. EO polarization rotation [142] and acousto-optic modulation

using piezoelectricity in LN [143–146] can be realized to electronically control the polarization and frequency on the chip. Scaling such systems could enable new applications in analog, sensing, and quantum photonics.

6. PERFORMANCE COMBINED WITH COMPLEXITY

Moving forward, LN EO devices have been and will continuously be improved in both performance and circuit complexity (Fig. 6), opening up many exciting new areas of applications. Using the design concepts for basic phase modulation elements shown in Figs. 2 and 3, a range of fundamental building blocks for a complex EO circuit, including phase modulators [87], intensity modulators, microring modulators [46,48,50,54–56,60,73,77,82,118,147,148], photonic crystal modulators [149], and Bragg grating-based modulators [150,151], have been demonstrated.

On the one hand, further improving the performance of these individual components could move them closer to practical applications. For example, improving the voltage and bandwidth could provide significant power reductions in datacom or telecom scenarios. Further reducing the coupling loss and increasing the optical power handling capabilities, could lead to paradigm shifts in analog photonics links [119] such as radio-over-fiber systems [152], RF beamforming [153], and imaging applications [154]. Extending functionalities of these basic EO elements can enable applications such as EO comb generation and EO modulation at visible [42] and mid-infrared wavelengths [155].

On the other hand, further increasing the PIC complexity could lead to large-scale, high-speed, low-power photonic switching networks [156] that can be used for data switching [157], photonic neural networks [158], photonic quantum computing [159,160], and fast photon control in ion-trap quantum systems [161].

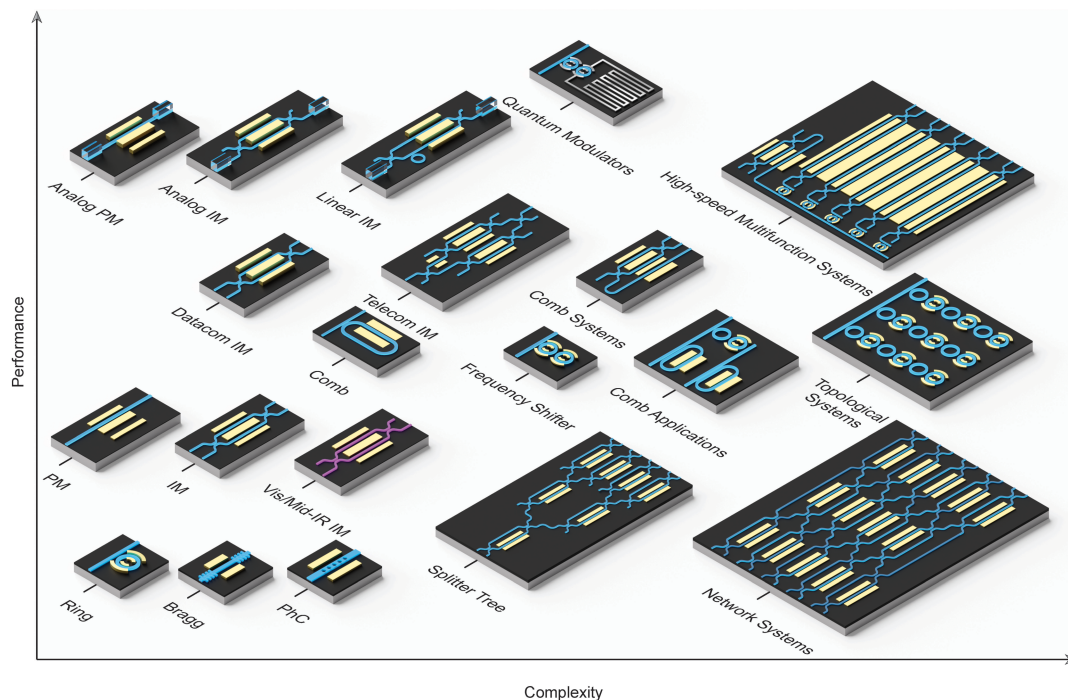


Fig. 6. Complexity and performance development prospects for thin-film lithium niobate modulators. A higher complexity indicates a larger number and/or more diversified optical elements. IM, intensity modulators; PM, phase modulators; Bragg, cavity-like modulators based on Bragg gratings; PhC, photonic crystal cavity modulators.

With both improved performance and circuit complexity, we can envisage the development of a new generation of integrated EO systems with unique functionalities. For example, integrating additional structures with the already highly performing modulators could lead to drastically improved modulation linearity, ideally suited for analog photonic links [8,122]; coherently driving few coupled microring modulator systems could lead to low-insertion-loss and high-efficiency frequency shifters [162]; and further integrating such coupled resonator systems with superconducting electrical circuits could enable a quantum coherent interface between optical and microwave photons [163,164]. Cascading intensity and phase modulators could lead to flat and efficient EO comb generators [151], and a pair of EO combs with a frequency shifter [162,165] can be used to form an aliasing-free dual-comb subsystem [166]. Ultimately, large-scale high-performance integrated LN circuits (top right of Fig. 6) could enable novel photonic phenomena and functionalities such as topological control which uniquely manipulate the frequency and momentum of light [167,168]. These large-scale PICs can also allow more compact and power-efficient optical subsystems. For example, a fully integrated wavelength-division multiplexed optical transmitter system could be realized by monolithically integrating a flat and high-efficiency comb generator with a coherent modulator array, as envisaged by several earlier works [169,170].

7. CONCLUSIONS

In this review, we have shown that integrated thin-film LN modulators are a promising solution for next-generation EO interface owing to its all-around performances and high potential for scalability. The reduced power consumption and high bandwidth of thin-film LN EOMs could have an immediate impact on the established applications in telecom, datacom, and analog photonics, with the prospect of providing disruptive solutions for quantum photonics, sensing, and artificial intelligence applications. To bring current research and EOM demonstrations into practical solutions, it is critical to achieve an efficient interface with the outside world by either optimized fiber–chip coupling or hybrid integration to other platforms. This will allow individual LN components to start manifesting their performance edges at the system level.

Future integrated EOMs and EO circuits demand ultrahigh speed, low power consumption, and diverse functionalities that thin-film LN promises to offer. While it is under intense research

on how exactly to connect thin-film LN to the rest of the photonics modality under techno-economic constraint, the outlook for full-fledged thin-film LN EO circuits is unparalleled—the combined low-loss passive optic, electro-optic, acousto-optic, and non-linear optic functionality on a monolithic material platform provides an extremely powerful toolbox that we are just starting to piece together.

APPENDIX A

1. MODULATOR FIGURES-OF-MERIT DEFINITION

We clarify our definitions for the half-wave voltage, EO bandwidth, extinction ratio, and insertion loss. The half-wave voltage V_π is defined as the voltage required to change the phase of light in a modulator by π . In an intensity modulator, this refers to the relative phase change between the two MZI arms (Fig. 7). Note that V_π is truly meaningful when the frequency of the measurement is specified as the voltage, which could vary drastically for different testing frequencies due to RF loss, impedance, velocity matching, photorefractive effect, etc.

The EO bandwidth of a modulator is commonly defined as either the 3 dB or 6 dB roll-off in the EO response curve of a modulator relative to a reference frequency (e.g., at 1 GHz) where V_π is defined (Fig. 7). The 3 dB (6 dB) point corresponds to an increase in V_π by a factor of $\sqrt{2}$ (2) from the reference lower frequency. The “useful bandwidth” is somewhat arbitrary, since a smooth response beyond the 6 dB roll-off may still be interesting for certain applications. The cutoff frequency refers to a sharp roll-off in response beyond certain frequencies due to, e.g., velocity mismatch. The extinction of a modulator specifies the ratio between the maximum and the minimum transmissions in the modulator transfer function (Fig. 7). Note that while this number is commonly only specified for low frequencies, high-frequency performances may vary especially in the presence of modulation-induced absorption.

The IL is the amount of optical power loss through the modulator. Here we define the insertion loss as the excessive loss from a modulator when it is biased at the maximum transmission (Fig. 7). In this case, an ideal modulator can have zero excessive loss. In other definitions that are appropriate for, for example, calculating link losses (which we did not use in this paper), insertion loss may include the unavoidable loss from the modulator transfer function, such as an extra 3 dB for an intensity modulator or voltage-dependent modulation loss for an operating modulator biased close to null transmission.

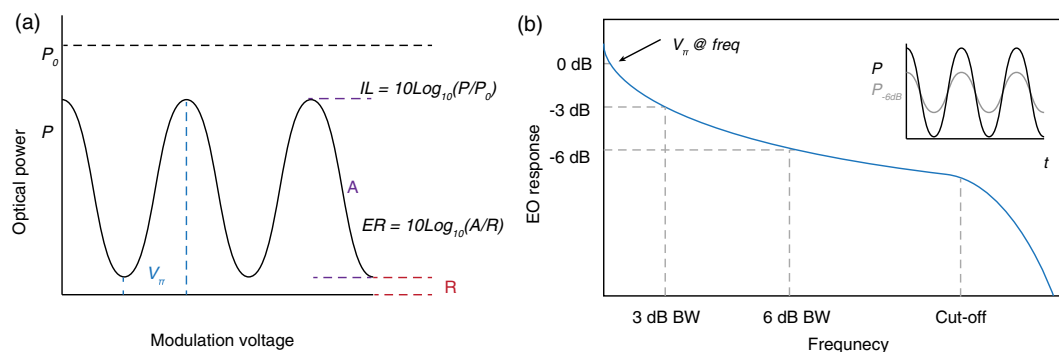
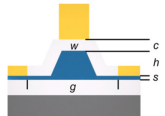
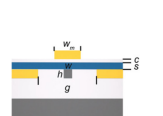
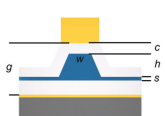
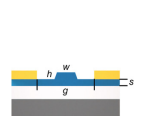
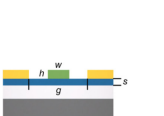


Fig. 7. Definition of various intensity modulator performance metrics. (a) Optical transmission spectrum of a Mach–Zehnder interferometer modulator with various parameters. IL is the insertion loss; ER is the extinction ratio; V_π is the half-wave voltage. (b) Typical electro-optic response curve of a modulator. The vertical axis is the ratio of the output electrical power on the photodetector normalized to a low-frequency response at a specified frequency (V_π @freq).

Table 1. Simulated Electro-Optic Efficiencies for Various Modulator Designs

Type	Z-Cut Monolithic	Z-Cut Hybrid	Z-Cut Buried Ground	X-Cut Monolithic	X-Cut Hybrid
Geometry					
Slab thickness (s)	300 nm	1.5 μm	1.5 μm	300 nm	300 nm
Ridge height (h)	1.2 μm	220 nm (Si)	1.2 μm	300 nm	300 nm (Si_3N_4)
Ridge width (w)	800 nm	400 nm (Si)	800 nm	800 nm	2 μm (Si_3N_4)
Metal gap (g)	3.2 μm	3.4 μm	3.2 μm	5 μm	6.5 μm
Cladding thickness (c)	700 nm	200 nm	700 nm	800 nm (not shown)	800 nm (not shown)
Substrate	Si	Si	Si	Si	Si
$V_\pi \cdot L$ (push-pull)	2.05 V \cdot cm	5.3 V \cdot cm	2.6 V \cdot cm	2.25 V \cdot cm	3.6 V \cdot cm
Electrode geometry	Differential GSGSG	Differential GSGSG	Differential GSGSG	GSG	GSG

2. MODULATION EFFICIENCY OF EXAMPLE DESIGNS

Here we provide a few examples of EO shifter designs with x - and z -cut geometries. The goal is to quantify typical $V_\pi \cdot L$ values under similar optical loss constraint. For a full high-speed EOM design, velocity matching, impedance and RF loss should be considered together with $V_\pi \cdot L$. To calculate $V_\pi \cdot L$, we first simulated the optical modes using the finite element method (Lumerical). While narrower gaps can reduce $V_\pi \cdot L$, this comes at the expense of added optical loss due to metal absorption. We choose the metal gap by finding the distance at which the added loss due to metal absorption is <0.2 dB/cm. The RF mode is simulated at 10 GHz using finite element method (Ansys HFSS software). We performed the EO overlap [63] to obtain RF $V_\pi \cdot L$ for each modulator design, which assumes a push-pull configuration. Note that it is possible to further optimize each modulator design and reduced $V_\pi \cdot L$ by methods such as fine-tuning waveguide geometry, adding dielectric buffer layers, and choosing dielectric material.

3. LIST OF STATE OF THE ART DISCUSSED IN THE TEXT

In Table 2, we list the selected samples of EO modulator used for benchmarking in Fig. 5. Owing to the varying reporting

Table 2. List of Electro-Optic Modulators Used in Fig. 5

Type	V_p (V)	L (mm)	$V_p L$ (V \cdot cm)	a (dB/cm)	BW (GHz)	Ref.
Hybrid	13.34	5	6.67	1.6	30	[48] ^a
Hybrid	13.4	5	6.7	0.6	106	[59]
Hybrid	6.8	6	4	5	—	[29]
Hybrid	6.3	6	3.8	1.2	1	[52]
Hybrid	3.9	8	3.1	1.2	33	[57] ^a
Hybrid	1.3	24	3.12	0.28	29	[75]
Hybrid	2.5	12	3	7	8	[46]
Monolithic	3.5	20	7	0.3	40	[87] ^b
Monolithic	21.5	1.35	2.9	15	—	[97]
Monolithic	12	4.5	5.3	3	—	[98]
Hybrid/monolithic	7.4	3	2.2	0.98	70	[50]
Hybrid/monolithic	5.1	5	2.5	0.98	70	[50]
Monolithic	4.4	5	2.2	0.3	100	[56]

(Table continued)

Type	V_p (V)	L (mm)	$V_p L$ (V \cdot cm)	a (dB/cm)	BW (GHz)	Ref.
Monolithic	2.3	10	2.3	0.3	80	[56]
Monolithic	1.4	20	2.8	0.3	45	[56]
Monolithic	1.5	15	2.25	0.5	20	[77]
Hybrid/monolithic	12	1	1.2	0.3	17.5	[89] ^{a,c}
Hybrid/monolithic	8.4	3	2.52	0.3	67	[89] ^a
Monolithic	2.6	12	3.1	0.3	56	[82] ^a
Monolithic	9	2	1.8	3	15	[54]
Monolithic	3.8	15	5.7	7	20	[58] ^c
Monolithic	1.9	13	2.5	0.15	48	[74]
Monolithic	3.1	7.5	2.3	0.15	70	[74]
Monolithic	9.4	10	9.4	1	40	[73] ^c
SOI	7	2	1.4	22	58	[90]
SOI	10.7	1.5	1.6	24	22.5	[101]
SOI	7.25	4.5	3.3	15	32	[93]
SOI	4.1	3.9	1.6	17.5	21	[91]
SOI	6.3	1.9	1.2	29.5	30	[91]
InP	1.5	4	1.2	1.5	80	[80] ^d
InP	0.77	10	0.77	2.5	40	[79]
Plasmonics	5.4	0.015	0.008	6400	500	[95]
Plasmonics	3	0.02	0.006	5000	500	[83]
Plasmonics	7.3	0.015	0.01	6600	100	[81]
SOH	1.6	0.6	0.1	19	50	[85]
SOH	0.21	1.5	0.03	39	20	[94]
SOH	1.48	0.28	0.04	25	40	[92]
SOH	1.8	8	1.4	2.2	68	[86]
BTO/Si	2.3	1	0.2	5.8	2	[84]
AlGaAs	1	1	0.1	4.5	—	[88]
Legacy LN	2.2	>40 (est)	>8.8	—	10	[99]
Legacy LN	5.5	>40 (est)	>20	—	35	[99]
Legacy LN	2.9	>40 (est)	>11	—	25	[100]
Legacy LN	3.5	>40 (est)	>14	—	35	[96]
Legacy LN	1.2	>40 (est)	>9	—	30	[23]

^aLoss estimated from the same group using similar technologies.^bRequires differential drive voltage.^cDouble-pass modulator V_π and $V_\pi L$ doubled in Fig. 5 to reflect single pass performance.^dVoltage doubled in Fig. 5 to reflect differential drive.

conventions in each reference (e.g. V_π can be defined at different frequencies), the listed data is intended to show a trend, instead of being used for exact value comparison.

Funding. Harvard Quantum Initiative; Harvard University; Research Grants Council, University Grants Committee (21208219); City University of Hong Kong (9610402, 9610455, 9667182); National Science Foundation; Air Force Office of Scientific Research; Army Research Laboratory; Raytheon Company; Nokia Bell Labs; Rockwell Collins; Google.

Acknowledgment. Cheng Wang is supported by Research Grant Council and City University of Hong Kong. Di Zhu is supported by the Harvard Quantum Initiative (HQI) postdoctoral fellowship. Marko Lončar would like to acknowledge NSF, AFOSR, ARL, Raytheon, Nokia Bell Labs, Rockwell Collins, and Google.

Disclosures. MZ, PK: HyperLight Corporation (I,E,P); CW, ML: HyperLight Corporation (F,I,C).

Data Availability. Data underlying the results presented in this paper are not publicly available at this time but may be obtained from the authors upon reasonable request.

REFERENCES

- P. J. Winzer, D. T. Neilson, and A. R. Chraplyvy, "Fiber-optic transmission and networking: the previous 20 and the next 20 years [Invited]," *Opt. Express* **26**, 24190–24239 (2018).
- Broadcom, "25.6 Tb/s StrataXGS Tomahawk 4 Ethernet switch series," <https://www.broadcom.com/products/ethernet-connectivity/switching/strataxgs/bcm56990-series>.
- H. Hou, "Industry-first co-packaged optics Ethernet switch solution with Intel silicon photonics," <https://itpeernetwork.intel.com/optics-ethernet-solution/#gs.ft2f7o>.
- Y. Yue, Q. Wang, and J. Anderson, "Experimental investigation of 400 Gb/s data center interconnect using unamplified high-baud-rate and high-order QAM single-carrier signal," *Appl. Sci.* **9**, 2455 (2019).
- C. Linghao, S. Aditya, and A. Nirmalathas, "An exact analytical model for dispersive transmission in microwave fiber-optic links using Mach-Zehnder external modulator," *IEEE Photonics Technol. Lett.* **17**, 1525–1527 (2005).
- L. Duvillaret, S. Rialland, and J.-L. Coutaz, "Electro-optic sensors for electric field measurements. I. Theoretical comparison among different modulation techniques," *J. Opt. Soc. Am. B* **19**, 2692–2703 (2002).
- H.-P. Lo, T. Ikuta, N. Matsuda, T. Honjo, and H. Takesue, "Electro-optic modulators for photonic quantum information processing," *Proc. SPIE* **11195**, 111950P (2019).
- X. Xiaobo, J. Khurgin, K. Jin, and F. Chow, "Linearized Mach-Zehnder intensity modulator," *IEEE Photonics Technol. Lett.* **15**, 531–533 (2003).
- M. Gimeno-Segovia, H. Cable, G. J. Mendoza, P. Shadbolt, J. W. Silverstone, J. Carolan, M. G. Thompson, J. L. O'Brien, and T. Rudolph, "Relative multiplexing for minimising switching in linear-optical quantum computing," *New J. Phys.* **19**, 063013 (2017).
- R. Hamerly, L. Bernstein, A. Sludds, M. Soljačić, and D. Englund, "Large-scale optical neural networks based on photoelectric multiplication," *Phys Rev X* **9**, 021032 (2019).
- G. T. Reed and A. P. Knights, *Silicon Photonics: An Introduction* (Wiley, 2004).
- B. Jalali and S. Fathpour, "Silicon photonics," *J. Lightwave Technol.* **24**, 4600–4615 (2006).
- G. T. Reed, G. Mashanovich, F. Y. Gardes, and D. J. Thomson, "Silicon optical modulators," *Nat. Photonics* **4**, 518–526 (2010).
- D. Thomson, A. Zilkie, J. E. Bowers, T. Komljenovic, G. T. Reed, L. Vivien, D. Marris-Morini, E. Cassan, L. Viot, J.-M. Fédéli, J.-M. Hartmann, J. H. Schmid, D.-X. Xu, F. Boeuf, P. O'Brien, G. Z. Mashanovich, and M. Nedeljkovic, "Roadmap on silicon photonics," *J. Opt.* **18**, 073003 (2016).
- M. Smit, K. Williams, and J. van der Tol, "Past, present, and future of InP-based photonic integration," *APL Photonics* **4**, 050901 (2019).
- E. L. Wooten, K. M. Kissa, A. Yi-Yan, E. J. Murphy, D. A. Lafaw, P. F. Hallemeier, D. Maack, D. V. Attanasio, D. J. Fritz, G. J. McBrien, and D. E. Bossi, "A review of lithium niobate modulators for fiber-optic communications systems," *IEEE J. Sel. Top. Quantum Electron.* **6**, 69–82 (2000).
- G. Roelkens, L. Liu, D. Liang, R. Jones, A. Fang, B. Koch, and J. Bowers, "III-V/silicon photonics for on-chip and intra-chip optical interconnects," *Laser Photonics Rev.* **4**, 751–779 (2010).
- O. Marshall, M. Hsu, Z. Wang, B. Kunert, C. Koos, and D. V. Thourhout, "Heterogeneous integration on silicon photonics," *Proc. IEEE* **106**, 2258–2269 (2018).
- R. S. Weis and T. K. Gaylord, "Lithium niobate: summary of physical properties and crystal structure," *Appl. Phys. A* **37**, 191–203 (1985).
- K.-K. Wong, *Properties of Lithium Niobate* (IET, 2002).
- "Fujitsu 100G/400G LN modulator," <https://www.fujitsu.com/jp/group/foc/en/products/devices/ln/indexig5.html>.
- R. W. Boyd, *Nonlinear Optics* (Elsevier, 2008).
- M. Doi, M. Sugiyama, K. Tanaka, and M. Kawai, "Advanced LiNbO₃ optical modulators for broadband optical communications," *IEEE J. Sel. Top. Quantum Electron.* **12**, 745–750 (2006).
- J. T. A. Carriere, J. A. Frantz, B. R. West, S. Honkanen, and R. K. Kostuk, "Bend loss effects in diffused, buried waveguides," *Appl. Opt.* **44**, 1698–1703 (2005).
- M. Bruel, "Silicon on insulator material technology," *Electron. Lett.* **31**, 1201–1202 (1995).
- P. Rabiei and P. Gunter, "Optical and electro-optical properties of sub-micrometer lithium niobate slab waveguides prepared by crystal ion slicing and wafer bonding," *Appl. Phys. Lett.* **85**, 4603–4605 (2004).
- M. Levy, R. M. Osgood, R. Liu, L. E. Cross, G. S. Cargill, A. Kumar, and H. Bakhru, "Fabrication of single-crystal lithium niobate films by crystal ion slicing," *Appl. Phys. Lett.* **73**, 2293–2295 (1998).
- H. Han, L. Cai, and H. Hu, "Optical and structural properties of single-crystal lithium niobate thin film," *Opt. Mater.* **42**, 47–51 (2015).
- P. Rabiei, J. Ma, S. Khan, J. Chiles, and S. Fathpour, "Heterogeneous lithium niobate photonics on silicon substrates," *Opt. Express* **21**, 25573–25581 (2013).
- K. Noguchi, O. Mitomi, H. Miyazawa, and S. Seki, "A broadband Ti:LiNbO₃ optical modulator with a ridge structure," *J. Lightwave Technol.* **13**, 1164–1168 (1995).
- G. Ulliac, V. Calero, A. Ndao, F. I. Baida, and M.-P. Bernal, "Argon plasma inductively coupled plasma reactive ion etching study for smooth sidewall thin film lithium niobate waveguide application," *Opt. Mater.* **53**, 1–5 (2016).
- H. Nagata, N. Mitsugi, K. Shima, M. Tamai, and E. M. Haga, "Growth of crystalline LiF on CF₄ plasma etched LiNbO₃ substrates," *J. Cryst. Growth* **187**, 573–576 (1998).
- J. Lin, Y. Xu, Z. Fang, M. Wang, J. Song, N. Wang, L. Qiao, W. Fang, and Y. Cheng, "Fabrication of high-Q lithium niobate microresonators using femtosecond laser micromachining," *Sci. Rep.* **5**, 8072 (2015).
- J. Wang, F. Bo, S. Wan, W. Li, F. Gao, J. Li, G. Zhang, and J. Xu, "High-Q lithium niobate microdisk resonators on a chip for efficient electro-optic modulation," *Opt. Express* **23**, 23072–23078 (2015).
- M. Zhang, C. Wang, R. Cheng, A. Shams-Ansari, and M. Lončar, "Monolithic ultra-high-Q lithium niobate microring resonator," *Optica* **4**, 1536–1537 (2017).
- I. Krasnokutskaya, J.-L. J. Tamasco, X. Li, and A. Peruzzo, "Ultra-low loss photonic circuits in lithium niobate on insulator," *Opt. Express* **26**, 897–904 (2018).
- R. Wolf, I. Breunig, H. Zappe, and K. Buse, "Scattering-loss reduction of ridge waveguides by sidewall polishing," *Opt. Express* **26**, 19815–19820 (2018).
- R. Wu, J. Zhang, N. Yao, W. Fang, L. Qiao, Z. Chai, J. Lin, and Y. Cheng, "Lithium niobate micro-disk resonators of quality factors above 10⁷," *Opt. Lett.* **43**, 4116–4119 (2018).
- Z. Gong, X. Liu, Y. Xu, M. Xu, J. B. Surya, J. Lu, A. Bruch, C. Zou, and H. X. Tang, "Soliton microcomb generation at 2 μm in z-cut lithium niobate microring resonators," *Opt. Lett.* **44**, 3182–3185 (2019).
- J.-X. Zhou, J. Lin, M. Wang, W. Chu, W.-B. Li, D.-F. Yin, L. Deng, Z.-W. Fang, J.-H. Zhang, R.-B. Wu, and Y. Cheng, "Electro-optically switchable optical true delay lines of meter-scale lengths fabricated on lithium niobate on insulator using photolithography assisted chemo-mechanical etching," *Chin. Phys. Lett.* **37**, 084201 (2020).
- K. Luke, P. Kharel, C. Reimer, L. He, M. Loncar, and M. Zhang, "Wafer-scale low-loss lithium niobate photonic integrated circuits," *Opt. Express* **28**, 24452–24458 (2020).
- B. Desiatov, A. Shams-Ansari, M. Zhang, C. Wang, and M. Lončar, "Ultra-low-loss integrated visible photonics using thin-film lithium niobate," *Optica* **6**, 380–384 (2019).
- Y. He, Q.-F. Yang, J. Ling, R. Luo, H. Liang, M. Li, B. Shen, H. Wang, K. Vahala, and Q. Lin, "Self-starting bi-chromatic LiNbO₃ soliton microcomb," *Optica* **6**, 1138–1144 (2019).

44. S. Y. Siew, E. J. H. Cheung, H. Liang, A. Bettiol, N. Toyoda, B. Alshehri, E. Dogheche, and A. J. Danner, "Ultra-low loss ridge waveguides on lithium niobate via argon ion milling and gas clustered ion beam smoothening," *Opt. Express* **26**, 4421–4430 (2018).
45. S. Li, L. Cai, Y. Wang, Y. Jiang, and H. Hu, "Waveguides consisting of single-crystal lithium niobate thin film and oxidized titanium stripe," *Opt. Express* **23**, 24212–24219 (2015).
46. S. Jin, L. Xu, H. Zhang, and Y. Li, "LiNbO₃ thin-film modulators using silicon nitride surface ridge waveguides," *IEEE Photonics Technol. Lett.* **28**, 736–739 (2016).
47. P. O. Weigel, M. Savanier, C. T. DeRose, A. T. Pomerene, A. L. Starbuck, A. L. Lentine, V. Stenger, and S. Mookherjea, "Lightwave circuits in lithium niobate through hybrid waveguides with silicon photonics," *Sci. Rep.* **6**, 22301 (2016).
48. N. Boynton, H. Cai, M. Gehl, S. Arterburn, C. Dallo, A. Pomerene, A. Starbuck, D. Hood, D. C. Trotter, T. Friedmann, C. T. DeRose, and A. Lentine, "A heterogeneously integrated silicon photonic/lithium niobate travelling wave electro-optic modulator," *Opt. Express* **28**, 1868–1884 (2020).
49. K. K. Mehta, G. N. West, and R. J. Ram, "SiN-on-LiNbO₃ integrated optical modulation at visible wavelengths," in *Conference on Lasers and Electro-Optics (CLEO)*, OSA Technical Digest (2017), paper STU3N.7.
50. M. He, M. Xu, Y. Ren, J. Jian, Z. Ruan, Y. Xu, S. Gao, S. Sun, X. Wen, L. Zhou, L. Liu, C. Guo, H. Chen, S. Yu, L. Liu, and X. Cai, "High-performance hybrid silicon and lithium niobate Mach-Zehnder modulators for 100 Gbit s⁻¹ and beyond," *Nat. Photonics* **13**, 359–364 (2019).
51. L. Chen, Q. Xu, M. G. Wood, and R. M. Reano, "Hybrid silicon and lithium niobate electro-optical ring modulator," *Optica* **1**, 112–118 (2014).
52. A. Rao, A. Patil, J. Chiles, M. Malinowski, S. Novak, K. Richardson, P. Rabiei, and S. Fathpour, "Heterogeneous microring and Mach-Zehnder modulators based on lithium niobate and chalcogenide glasses on silicon," *Opt. Express* **23**, 22746–22752 (2015).
53. L. Chang, Y. Li, N. Volet, L. Wang, J. Peters, and J. E. Bowers, "Thin film wavelength converters for photonic integrated circuits," *Optica* **3**, 531–535 (2016).
54. C. Wang, M. Zhang, B. Stern, M. Lipson, and M. Lončar, "Nanophotonic lithium niobate electro-optic modulators," *Opt. Express* **26**, 1547–1555 (2018).
55. A. N. R. Ahmed, S. Nelan, S. Shi, P. Yao, A. Mercante, and D. W. Prather, "Subvolt electro-optical modulator on thin-film lithium niobate and silicon nitride hybrid platform," *Opt. Lett.* **45**, 1112–1115 (2020).
56. C. Wang, M. Zhang, X. Chen, M. Bertrand, A. Shams-Ansari, S. Chandrasekhar, P. Winzer, and M. Lončar, "Integrated lithium niobate electro-optic modulators operating at CMOS-compatible voltages," *Nature* **562**, 101–104 (2018).
57. A. Rao, A. Patil, P. Rabiei, A. Honardoost, R. DeSalvo, A. Paoletta, and S. Fathpour, "High-performance and linear thin-film lithium niobate Mach-Zehnder modulators on silicon up to 50 GHz," *Opt. Lett.* **41**, 5700–5703 (2016).
58. A. J. Mercante, S. Shi, P. Yao, L. Xie, R. M. Weikle, and D. W. Prather, "Thin film lithium niobate electro-optic modulator with terahertz operating bandwidth," *Opt. Express* **26**, 14810–14816 (2018).
59. P. O. Weigel, J. Zhao, K. Fang, H. Al-Rubaye, D. Trotter, D. Hood, J. Mudrick, C. Dallo, A. T. Pomerene, A. L. Starbuck, C. T. DeRose, A. L. Lentine, G. Rebeiz, and S. Mookherjea, "Bonded thin film lithium niobate modulator on a silicon photonics platform exceeding 100 GHz 3-dB electrical modulation bandwidth," *Opt. Express* **26**, 23728–23739 (2018).
60. A. Rao, M. Malinowski, A. Honardoost, J. R. Talukder, P. Rabiei, P. Delyett, and S. Fathpour, "Second-harmonic generation in periodically-poled thin film lithium niobate wafer-bonded on silicon," *Opt. Express* **24**, 29941–29947 (2016).
61. A. Guarino, G. Poberaj, D. Rezzonico, R. Degl'Innocenti, and P. Günter, "Electro-optically tunable microring resonators in lithium niobate," *Nat. Photonics* **1**, 407–410 (2007).
62. P. Rabiei and W. H. Steier, "Lithium niobate ridge waveguides and modulators fabricated using smart guide," *Appl. Phys. Lett.* **86**, 161115 (2005).
63. N. Dagli, *High-speed Photonic Devices* (CRC Press, 2006).
64. D. Pozar, *Microwave Engineering*, 4th ed. (Wiley, 2020).
65. F. Koyama and K. Iga, "Frequency chirping in external modulators," *J. Lightwave Technol.* **6**, 87–93 (1988).
66. A. Honardoost, F. A. Juneghani, R. Safian, and S. Fathpour, "Towards subterahertz bandwidth ultracompact lithium niobate electrooptic modulators," *Opt. Express* **27**, 6495–6501 (2019).
67. N. Courjal, H. Porte, J. Hauden, P. Mollier, and N. Grossard, "Modeling and optimization of low chirp LiNbO₃ Mach-Zehnder modulators with an inverted ferroelectric domain section," *J. Lightwave Technol.* **22**, 1338–1343 (2004).
68. G. Ghione, *Semiconductor Devices for High-Speed Optoelectronics* (Cambridge University Press, 2009).
69. A. Chowdhury and L. McCaughan, "Figure of merit for near-velocity-matched traveling-wave modulators," *Opt. Lett.* **26**, 1317–1319 (2001).
70. J. A. Ibarra Fuste and M. C. Santos Blanco, "Bandwidth-length trade-off figures of merit for electro-optic traveling wave modulators," *Opt. Lett.* **38**, 1548–1550 (2013).
71. H. Hu, R. Ricken, and W. Sohler, "Lithium niobate photonic wires," *Opt. Express* **17**, 24261–24268 (2009).
72. G. Poberaj, H. Hu, W. Sohler, and P. Günter, "Lithium niobate on insulator (LNOI) for micro-photonics devices," *Laser Photonics Rev.* **6**, 488–503 (2012).
73. A. J. Mercante, P. Yao, S. Shi, G. Schneider, J. Murakowski, and D. W. Prather, "110 GHz CMOS compatible thin film LiNbO₃ modulator on silicon," *Opt. Express* **24**, 15590–15595 (2016).
74. M. Xu, M. He, H. Zhang, J. Jian, Y. Pan, X. Liu, L. Chen, X. Meng, H. Chen, Z. Li, X. Xiao, S. Yu, S. Yu, and X. Cai, "High-performance coherent optical modulators based on thin-film lithium niobate platform," *Nat. Commun.* **11**, 3911 (2020).
75. A. N. R. Ahmed, S. Shi, A. Mercante, S. Nelan, P. Yao, and D. W. Prather, "High-efficiency lithium niobate modulator for K band operation," *APL Photonics* **5**, 091302 (2020).
76. L. Chen, M. G. Wood, and R. M. Reano, "12.5 pm/V hybrid silicon and lithium niobate optical microring resonator with integrated electrodes," *Opt. Express* **21**, 27003–27010 (2013).
77. V. E. Stenger, J. Toney, A. PoNick, D. Brown, B. Griffin, R. Nelson, and S. Sriram, "Low loss and low V_π thin film lithium niobate on quartz electro-optic modulators," in *European Conference on Optical Communication (ECOC)* (2017), pp. 1–3.
78. M. Bahadori, Y. Yang, A. E. Hassanien, L. L. Goddard, and S. Gong, "Ultra-efficient and fully isotropic monolithic microring modulators in thin-film lithium niobate photonics platform," *Opt. Express* **28**, 29644–29661 (2020).
79. S. Dogru and N. Dagli, "0.77-V drive voltage electro-optic modulator with bandwidth exceeding 67 GHz," *Opt. Lett.* **39**, 6074–6077 (2014).
80. Y. Ogiso, J. Ozaki, Y. Ueda, H. Wakita, M. Nagatani, H. Yamazaki, M. Nakamura, T. Kobayashi, S. Kanazawa, Y. Hashizume, H. Tanobe, N. Nunoya, M. Ida, Y. Miyamoto, and M. Ishikawa, "480-GHz bandwidth and 1.5-V V_π InP-based IQ modulator," *J. Lightwave Technol.* **38**, 249–255 (2020).
81. B. Baeuerle, W. Heni, C. Hoessbacher, Y. Fedoryshyn, U. Koch, A. Josten, T. Watanabe, C. Uhl, H. Hettrich, D. L. Elder, L. R. Dalton, M. Möller, and J. Leuthold, "120 Gbd plasmonic Mach-Zehnder modulator with a novel differential electrode design operated at a peak-to-peak drive voltage of 178 mV," *Opt. Express* **27**, 16823–16832 (2019).
82. Y. Zhang, M. Xu, H. Zhang, M. Li, J. Jian, M. He, L. Chen, L. Wang, X. Cai, X. Xiao, and S. Yu, "220 Gbit/s optical PAM4 modulation based on lithium niobate on insulator modulator," in *45th European Conference on Optical Communication (ECOC)* (2019), pp. 1–4.
83. M. Burla, C. Hoessbacher, W. Heni, C. Haffner, Y. Fedoryshyn, D. Werner, T. Watanabe, H. Massler, D. L. Elder, L. R. Dalton, and J. Leuthold, "500 GHz plasmonic Mach-Zehnder modulator enabling sub-THz microwave photonics," *APL Photonics* **4**, 056106 (2019).
84. F. Eltes, C. Mai, D. Caimi, M. Kroh, Y. Popoff, G. Winzer, D. Petousi, S. Lischke, J. E. Ortmann, L. Czornomaz, L. Zimmermann, J. Fompeyrine, and S. Abel, "A BaTiO₃-based electro-optic Pockels modulator monolithically integrated on an advanced silicon photonics platform," *J. Lightwave Technol.* **37**, 1456–1462 (2019).
85. S. Wolf, H. Zwickel, C. Kieninger, M. Lauermann, W. Hartmann, Y. Kutuvantavida, W. Freude, S. Randel, and C. Koos, "Coherent modulation up to 100 GBd 16QAM using silicon-organic hybrid (SOH) devices," *Opt. Express* **26**, 220–232 (2018).

86. G.-W. Lu, J. Hong, F. Qiu, A. M. Spring, T. Kashino, J. Oshima, M.-A. Ozawa, H. Nawata, and S. Yokoyama, "High-temperature-resistant silicon-polymer hybrid modulator operating at up to 200 Gbit s⁻¹ for energy-efficient datacenters and harsh-environment applications," *Nat. Commun.* **11**, 4224 (2020).
87. T. Ren, M. Zhang, C. Wang, L. Shao, C. Reimer, Y. Zhang, O. King, R. Esman, T. Cullen, and M. Lončar, "An integrated low-voltage broadband lithium niobate phase modulator," *IEEE Photonics Technol. Lett.* **31**, 889–892 (2019).
88. P. Bhasker, J. Norman, J. Bowers, and N. Dagli, "Low voltage, high optical power handling capable, bulk compound semiconductor electro-optic modulators at 1550 nm," *J. Lightwave Technol.* **38**, 2308–2314 (2020).
89. M. Xu, W. Chen, M. He, X. Wen, Z. Ruan, J. Xu, L. Chen, L. Liu, S. Yu, and X. Cai, "Michelson interferometer modulator based on hybrid silicon and lithium niobate platform," *APL Photonics* **4**, 100802 (2019).
90. M. Li, L. Wang, X. Li, X. Xiao, and S. Yu, "Silicon intensity Mach-Zehnder modulator for single lane 100 Gb/s applications," *Photonics Res.* **6**, 109–116 (2018).
91. J. Zhou, J. Wang, L. Zhu, Q. Zhang, Q. Zhang, and J. Hong, "Silicon photonics carrier depletion modulators capable of 85 Gbaud 16QAM and 64 Gbaud 64QAM," in *Optical Fiber Communication Conference* (Optical Society of America, 2019), paper Tu2H.2.
92. C. Kieninger, C. Füllner, H. Zwickel, Y. Kutuvantavida, J. N. Kemal, C. Eschenbaum, D. L. Elder, L. R. Dalton, W. Freude, S. Randel, and C. Koos, "Silicon-organic hybrid (SOH) Mach-Zehnder modulators for 100 Gb/s PAM4 signaling with sub-1 dB phase-shifter loss," *Opt. Express* **28**, 24693–24707 (2020).
93. J. Lin, H. Sepéhran, L. A. Rusch, and W. Shi, "Single-carrier 72 Gbaud 32QAM and 84 Gbaud 16QAM transmission using a SiP IQ modulator with joint digital-optical pre-compensation," *Opt. Express* **27**, 5610–5619 (2019).
94. C. Kieninger, Y. Kutuvantavida, D. L. Elder, S. Wolf, H. Zwickel, M. Blaicher, J. N. Kemal, M. Laueremann, S. Randel, W. Freude, L. R. Dalton, and C. Koos, "Ultra-high electro-optic activity demonstrated in a silicon-organic hybrid modulator," *Optica* **5**, 739–748 (2018).
95. W. Heni, B. Baeuerle, H. Mardoyan, F. Jorge, J. M. Estaran, A. Koncewskowska, M. Riet, B. Duval, V. Nodjiadjim, M. Goix, J. Dupuy, M. Destraz, C. Hoessbacher, Y. Fedoryshyn, H. Xu, D. L. Elder, L. R. Dalton, J. Renaudier, and J. Leuthold, "Ultra-high-speed 2:1 digital selector and plasmonic modulator IM/DD transmitter operating at 222 Gbaud for intra-datacenter applications," *J. Lightwave Technol.* **38**, 2734–2739 (2020).
96. EOSpace, "40+ GB/S modulators," <https://www.eospace.com/product-summary-modulator>.
97. X. P. Li, K. X. Chen, and L. F. Wang, "Compact and electro-optic tunable interleaver in lithium niobate thin film," *Opt. Lett.* **43**, 3610–3613 (2018).
98. M. Jin, J.-Y. Chen, Y. M. Sua, and Y.-P. Huang, "High-extinction electro-optic modulation on lithium niobate thin film," *Opt. Lett.* **44**, 1265–1268 (2019).
99. Thorlabs, "Lithium niobate electro-optic modulators, fiber-coupled," https://www.thorlabs.com/newgrouppage9.cfm?objectgroup_id=3918.
100. Fujitsu, "Low drive voltage 40 Gb/s NRZ LiNbO₃ external modulator," <https://www.fujitsu.com/downloads/OPTCMP/lineup/40Gln/40Glnrz-catalog.pdf>.
101. Y. Zhu, F. Zhang, F. Yang, L. Zhang, X. Ruan, Y. Li, and Z. Chen, "Toward single lane 200 G optical interconnects with silicon photonic modulator," *J. Lightwave Technol.* **38**, 67–74 (2020).
102. W. P. Orlando, V. Forrest, Z. Jie, L. Huiyan, and M. Shayan, "Design of high-bandwidth, low-voltage and low-loss hybrid lithium niobate electro-optic modulators," *J. Phys. Photonics* **3**, 012001 (2020).
103. X. Liu, B. Xiong, C. Sun, Z. Hao, L. Wang, J. Wang, Y. Han, H. Li, J. Yu, and Y. Luo, "Low half-wave-voltage thin film LiNbO₃ electro-optic modulator based on a compact electrode structure," *Asia Communications and Photonics Conference/International Conference on Information Photonics and Optical Communications (ACP/IPOC)*, Beijing, China (24–27 October 2020), paper M4A.144.
104. P. Kharel, C. Reimer, K. Luke, L. He, and M. Zhang, "Breaking voltage-bandwidth limits in integrated lithium niobate modulators using microstructured electrodes," *Optica* **8**, 357–363 (2021).
105. M. Lee, "Dielectric constant and loss tangent in LiNbO₃ crystals from 90 to 147 GHz," *Appl. Phys. Lett.* **79**, 1342–1344 (2001).
106. X. Mu, S. Wu, L. Cheng, and H. Y. Fu, "Edge couplers in silicon photonic integrated circuits: a review," *Appl. Sci.* **10**, 1538 (2020).
107. C. Wang, M. Zhang, M. Yu, R. Zhu, H. Hu, and M. Loncar, "Monolithic lithium niobate photonic circuits for Kerr frequency comb generation and modulation," *Nat. Commun.* **10**, 978 (2019).
108. N. Yao, J. Zhou, R. Gao, J. Lin, M. Wang, Y. Cheng, W. Fang, and L. Tong, "Efficient light coupling between an ultra-low loss lithium niobate waveguide and an adiabatically tapered single mode optical fiber," *Opt. Express* **28**, 12416–12423 (2020).
109. I. Krasnokutskaya, J.-L. J. Tambsco, and A. Peruzzo, "Nanostructuring of LNOI for efficient edge coupling," *Opt. Express* **27**, 16578–16585 (2019).
110. C. Hu, A. Pan, T. Li, X. Wang, Y. Liu, S. Tao, C. Zeng, and J. Xia, "High-efficient coupler for thin-film lithium niobate waveguide devices," *Opt. Express* **29**, 5397–5406 (2021).
111. A. Kar, M. Bahadori, S. Gong, and L. L. Goddard, "Realization of alignment-tolerant grating couplers for z-cut thin-film lithium niobate," *Opt. Express* **27**, 15856–15867 (2019).
112. J. Jian, M. Xu, L. Liu, Y. Luo, J. Zhang, L. Liu, L. Zhou, H. Chen, S. Yu, and X. Cai, "High modulation efficiency lithium niobate Michelson interferometer modulator," *Opt. Express* **27**, 18731–18739 (2019).
113. Z. Chen, Y. Wang, Y. Jiang, R. Kong, and H. Hu, "Grating coupler on single-crystal lithium niobate thin film," *Opt. Mater.* **72**, 136–139 (2017).
114. L. Cai and G. Piazza, "Low-loss chirped grating for vertical light coupling in lithium niobate on insulator," *J. Opt.* **21**, 065801 (2019).
115. H. Lin, S. Gao, Y. Luo, J. Jian, M. He, X. Liu, X. Zhong, Z. Chen, L. Chen, and X. Cai, "Ultra-high-efficiency apodized grating couplers on hybrid amorphous silicon and lithium niobate platform," *Asia Communications and Photonics Conference (ACPC)*, Chengdu, China (2–5 November 2019), paper M4A.238.
116. A. Pan, C. Hu, C. Zeng, and J. Xia, "Fundamental mode hybridization in a thin film lithium niobate ridge waveguide," *Opt. Express* **27**, 35659–35669 (2019).
117. K. Suzuki, G. Cong, K. Tanizawa, S.-H. Kim, K. Ikeda, S. Namiki, and H. Kawashima, "Ultra-high-extinction-ratio 2 × 2 silicon optical switch with variable splitter," *Opt. Express* **23**, 9086–9092 (2015).
118. Z. Yu, X. Xi, J. Ma, H. K. Tsang, C.-L. Zou, and X. Sun, "Photonic integrated circuits with bound states in the continuum," *Optica* **6**, 1342–1348 (2019).
119. D. Marpaung, J. Yao, and J. Capmany, "Integrated microwave photonics," *Nat. Photonics* **13**, 80–90 (2019).
120. A. Karim and J. Devenport, "Noise figure reduction in externally modulated analog fiber-optic links," *IEEE Photonics Technol. Lett.* **19**, 312–314 (2007).
121. L. Chen, J. Chen, J. Nagy, and R. M. Reano, "Highly linear ring modulator from hybrid silicon and lithium niobate," *Opt. Express* **23**, 13255–13264 (2015).
122. D. J. M. Sabido, M. Tabara, T. K. Fong, L. Chung-Li, and L. G. Kazovsky, "Improving the dynamic range of a coherent AM analog optical link using a cascaded linearized modulator," *IEEE Photonics Technol. Lett.* **7**, 813–815 (1995).
123. P. Günter and J.-P. Huignard, *Photorefractive Materials and Their Applications* (Springer, 2007).
124. J. P. Salvestrini, L. Guilbert, M. Fontana, M. Abarkan, and S. Gille, "Analysis and control of the DC drift in LiNbO₃ based Mach-Zehnder modulators," *J. Lightwave Technol.* **29**, 1522–1534 (2011).
125. H. Nagata, N. F. O. Brien, W. R. Bosenberg, G. L. Reiff, and K. R. Voisine, "DC-voltage-induced thermal shift of bias point in LiNbO₃ optical modulators," *IEEE Photonics Technol. Lett.* **16**, 2460–2462 (2004).
126. H. Jiang, R. Luo, H. Liang, X. Chen, Y. Chen, and Q. Lin, "Fast response of photorefractive in lithium niobate microresonators," *Opt. Lett.* **42**, 3267–3270 (2017).
127. X. Sun, H. Liang, R. Luo, W. C. Jiang, X.-C. Zhang, and Q. Lin, "Nonlinear optical oscillation dynamics in high-Q lithium niobate microresonators," *Opt. Express* **25**, 13504–13516 (2017).
128. L. Moretti, M. Iodice, F. G. Della Corte, and I. Rendina, "Temperature dependence of the thermo-optic coefficient of lithium niobate, from 300 to 515 K in the visible and infrared regions," *J. Appl. Phys.* **98**, 036101 (2005).
129. W. Jiang, F. M. Mayor, R. N. Patel, T. P. McKenna, C. J. Sarabalis, and A. H. Safavi-Naeini, "Nanobenders as efficient piezoelectric actuators

- for widely tunable nanophotonics at CMOS-level voltages," *Commun. Phys.* **3**, 156 (2020).
130. C. Wang, C. Langrock, A. Marandi, M. Jankowski, M. Zhang, B. Desiatov, M. M. Fejer, and M. Lončar, "Ultra-high-efficiency wavelength conversion in nanophotonic periodically poled lithium niobate waveguides," *Optica* **5**, 1438–1441 (2018).
 131. Y. Kong, F. Bo, W. Wang, D. Zheng, H. Liu, G. Zhang, R. Rupp, and J. Xu, "Recent progress in lithium niobate: optical damage, defect simulation, and on-chip devices," *Adv. Mater.* **32**, 1806452 (2020).
 132. F. Mondain, F. Brunel, X. Hua, E. Gouzien, A. Zavatta, T. Lunghi, F. Doutre, M. P. De Micheli, S. Tanzilli, and V. D'Auria, "Photorefractive effect in LiNbO₃-based integrated-optical circuits for continuous variable experiments," *Opt. Express* **28**, 23176–23188 (2020).
 133. H. Liang, R. Luo, Y. He, H. Jiang, and Q. Lin, "High-quality lithium niobate photonic crystal nanocavities," *Optica* **4**, 1251–1258 (2017).
 134. J. T. Nagy and R. M. Reano, "Reducing leakage current during periodic poling of ion-sliced x-cut MgO doped lithium niobate thin films," *Opt. Mater. Express* **9**, 3146–3155 (2019).
 135. X. Yan, Y. A. Liu, L. Ge, B. Zhu, J. Wu, Y. Chen, and X. Chen, "High optical damage threshold on-chip lithium tantalate microdisk resonator," *Opt. Lett.* **45**, 4100–4103 (2020).
 136. A. Alexandrovski, G. Foulon, L. Myers, R. Route, and M. Fejer, *UV and Visible Absorption in LiTaO₃* (SPIE, 1999).
 137. R. Safian, M. Teng, L. Zhuang, and S. Chakravarty, "Foundry-compatible thin film lithium niobate modulator with RF electrodes buried inside the silicon oxide layer of the SOI wafer," *Opt. Express* **28**, 25843–25857 (2020).
 138. Thorlabs, "Lithium niobate electro-optic modulators, fiber-coupled," https://www.nanoln.com/PRODUCTS_128978.html.
 139. J. Lu, J. B. Surya, X. Liu, A. W. Bruch, Z. Gong, Y. Xu, and H. X. Tang, "Periodically poled thin-film lithium niobate microring resonators with a second-harmonic generation efficiency of 250,000%/W," *Optica* **6**, 1455–1460 (2019).
 140. J. Zhao, C. Ma, M. Rüsing, and S. Mookherjee, "High quality entangled photon pair generation in periodically poled thin-film lithium niobate waveguides," *Phys. Rev. Lett.* **124**, 163603 (2020).
 141. J.-Y. Chen, C. Tang, Z.-H. Ma, Z. Li, Y. Meng Sua, and Y.-P. Huang, "Efficient and highly tunable second-harmonic generation in Z-cut periodically poled lithium niobate nanowaveguides," *Opt. Lett.* **45**, 3789–3792 (2020).
 142. J. Wu, Y. Huang, C. Lu, T. Ding, Y. Zheng, and X. Chen, "Tunable linear polarization-state generator of single photons on a lithium niobate chip," *Phys. Rev. Appl.* **13**, 064068 (2020).
 143. L. Shao, M. Yu, S. Maity, N. Sinclair, L. Zheng, C. Chia, A. Shams-Ansari, C. Wang, M. Zhang, K. Lai, and M. Lončar, "Microwave-to-optical conversion using lithium niobate thin-film acoustic resonators," *Optica* **6**, 1498–1505 (2019).
 144. C. J. Sarabalis, T. P. McKenna, R. N. Patel, R. Van Laer, and A. H. Safavi-Naeini, "Acousto-optic modulation in lithium niobate on sapphire," *APL Photonics* **5**, 086104 (2020).
 145. Z. Yu and X. Sun, "Acousto-optic modulation of photonic bound state in the continuum," *Light Sci. Appl.* **9**, 1 (2020).
 146. L. Cai, A. Mahmoud, M. Khan, M. Mahmoud, T. Mukherjee, J. Bain, and G. Piazza, "Acousto-optical modulation of thin film lithium niobate waveguide devices," *Photonics Res.* **7**, 1003–1013 (2019).
 147. A. J. Mercante, D. L. K. Eng, M. Konkol, P. Yao, S. Shi, and D. W. Prather, "Thin LiNbO₃ on insulator electro-optic modulator," *Opt. Lett.* **41**, 867–869 (2016).
 148. M. Zhang, C. Wang, X. Chen, M. Bertrand, A. Shams-Ansari, S. Chandrasekhar, P. Winzer, and M. Lončar, "Ultra-high bandwidth integrated lithium niobate modulators with record-low V_π," in *Optical Fiber Communication Conference* (2018), paper Th4A.5.
 149. M. Li, J. Ling, Y. He, U. A. Javid, S. Xue, and Q. Lin, "Lithium niobate photonic-crystal electro-optic modulator," *Nat. Commun.* **11**, 4123 (2020).
 150. M. R. Escalé, D. Pohl, A. Sergeev, and R. Grange, "Extreme electro-optic tuning of Bragg mirrors integrated in lithium niobate nanowaveguides," *Opt. Lett.* **43**, 1515–1518 (2018).
 151. M. Xu, M. He, X. Liu, Y. Pan, S. Yu, and X. Cai, "Integrated lithium niobate modulator and frequency comb generator based on Fabry-Perot resonators," in *CLEO: Science and Innovations* (Optical Society of America, 2020), paper JTh2B.27.
 152. A. M. Zin, M. S. Bongsu, S. M. Idrus, and N. Zulkifli, "An overview of radio-over-fiber network technology," in *International Conference on Photonics* (2010), pp. 1–3.
 153. S. Akiba, M. Oishi, Y. Nishikawa, K. Minoguchi, J. Hirokawa, and M. Ando, "Photonic architecture for beam forming of RF phased array antenna," *Optical Fiber Communication Conference*, San Francisco, California, USA, (9–13 March 2014), paper W2A.51.
 154. R. D. Martin, S. Shi, Y. Zhang, A. Wright, P. Yao, K. P. Shreve, C. A. Schuetz, T. E. Dillon, D. G. Mackrides, and C. E. Harry, "Video rate passive millimeter-wave imager utilizing optical upconversion with improved size, weight, and power," *Proc. SPIE* **9462**, 946209 (2015).
 155. J. Chiles and S. Fathpour, "Mid-infrared integrated waveguide modulators based on silicon-on-lithium-niobate photonics," *Optica* **1**, 350–355 (2014).
 156. G. I. Papadimitriou, C. Papazoglou, and A. S. Pomportsis, "Optical switching: switch fabrics, techniques, and architectures," *J. Lightwave Technol.* **21**, 384–405 (2003).
 157. Q. Cheng, S. Rumley, M. Bahadori, and K. Bergman, "Photonic switching in high performance datacenters [invited]," *Opt. Express* **26**, 16022–16043 (2018).
 158. N. C. Harris, J. Carolan, D. Bunandar, M. Prabhu, M. Hochberg, T. Baehr-Jones, M. L. Fanto, A. M. Smith, C. C. Tison, P. M. Alsing, and D. Englund, "Linear programmable nanophotonic processors," *Optica* **5**, 1623–1631 (2018).
 159. J. Carolan, C. Harrold, C. Sparrow, E. Martin-Lopez, N. J. Russell, J. W. Silverstone, P. J. Shadbolt, N. Matsuda, M. Oguma, M. Itoh, G. D. Marshall, M. G. Thompson, J. C. F. Matthews, T. Hashimoto, J. L. O'Brien, and A. Laing, "Universal linear optics," *Science* **349**, 711–716 (2015).
 160. J. Wang, F. Sciarrino, A. Laing, and M. G. Thompson, "Integrated photonic quantum technologies," *Nat. Photonics* **14**, 273–284 (2020).
 161. S. Debnath, N. M. Linke, C. Figgatt, K. A. Landsman, K. Wright, and C. Monroe, "Demonstration of a small programmable quantum computer with atomic qubits," *Nature* **536**, 63–66 (2016).
 162. Y. Hu, M. Yu, D. Zhu, N. Sinclair, A. Shams-Ansari, L. Shao, J. Holzgrafe, E. Puma, M. Zhang, and M. Loncar, "Reconfigurable electro-optic frequency shifter," arXiv:2005.09621 (2020).
 163. J. Holzgrafe, N. Sinclair, D. Zhu, A. Shams-Ansari, M. Colangelo, Y. Hu, M. Zhang, K. K. Berggren, and M. Lončar, "Cavity electro-optics in thin-film lithium niobate for efficient microwave-to-optical transduction," *Optica* **7**, 1714–1720 (2020).
 164. T. P. McKenna, J. D. Witmer, R. N. Patel, W. Jiang, R. Van Laer, P. Arrangoiz-Arriola, E. A. Wollack, J. F. Herrmann, and A. H. Safavi-Naeini, "Cryogenic microwave-to-optical conversion using a triply-resonant lithium niobate on sapphire transducer," *Optica* **7**, 1737–1745 (2020).
 165. C. Qin, H. Lu, B. Ercan, S. Li, and S. J. Ben Yoo, "Single-tone optical frequency shifting and nonmagnetic optical isolation by electro-optical emulsion of a rotating half-wave plate in a traveling-wave lithium niobate waveguide," *IEEE Photonics J.* **9**, 6600913 (2017).
 166. A. Shams-Ansari, M. Yu, Z. Chen, C. Reimer, M. Zhang, N. Picqué, and M. Lončar, "An integrated lithium-niobate electro-optic platform for spectrally tailored dual-comb spectroscopy," arXiv:2003.04533 (2020).
 167. Q. Lin, M. Xiao, L. Yuan, and S. Fan, "Photonic Weyl point in a two-dimensional resonator lattice with a synthetic frequency dimension," *Nat. Commun.* **7**, 13731 (2016).
 168. L. Yuan, Y. Shi, and S. Fan, "Photonic gauge potential in a system with a synthetic frequency dimension," *Opt. Lett.* **41**, 741–744 (2016).
 169. P. Marin-Palomo, J. N. Kemal, M. Karpov, A. Kordts, J. Pfeifle, M. H. P. Pfeiffer, P. Trocha, S. Wolf, V. Brasch, M. H. Anderson, R. Rosenberger, K. Vijayan, W. Freude, T. J. Kippenberg, and C. Koos, "Microresonator-based solitons for massively parallel coherent optical communications," *Nature* **546**, 274–279 (2017).
 170. J. Pfeifle, V. Brasch, M. Lauer, Y. Yu, D. Wegner, T. Herr, K. Hartinger, P. Schindler, J. Li, D. Hillerkuss, R. Schmogrow, C. Weimann, R. Holzwarth, W. Freude, J. Leuthold, T. J. Kippenberg, and C. Koos, "Coherent terabit communications with microresonator Kerr frequency combs," *Nat. Photonics* **8**, 375–380 (2014).